

MICROCOPY RESOLUTION TEST CHART  
NATIONAL BUREAU OF STANDARDS - 1963-A

ADA 112717

SECURITY CLASSIFICATION OF THIS PAGE (When Data Entered)

REPORT DOCUMENTATION PAGE		READ INSTRUCTIONS BEFORE COMPLETING FORM
1. REPORT NUMBER NRL Memorandum Report 4747	2. GOVT ACCESSION NO. AD-A112717	3. RECIPIENT'S CATALOG NUMBER
4. TITLE (and Subtitle) ABLATIVE ACCELERATION OF PLANAR TARGETS TO HIGH VELOCITIES	5. TYPE OF REPORT & PERIOD COVERED Interim report on a continuing NRL problem.	
	6. PERFORMING ORG. REPORT NUMBER	
7. AUTHOR(s) J. Grun*, S.P. Obenschain, B.H. Ripin, R.R. Whitlock, E.A. McLean, J. Gardner, M.J. Herbst, and J.A. Stamper	8. CONTRACT OR GRANT NUMBER(s)	
9. PERFORMING ORGANIZATION NAME AND ADDRESS Naval Research Laboratory Washington, DC 20375	10. PROGRAM ELEMENT, PROJECT, TASK AREA & WORK UNIT NUMBERS 47-0859-0-2	
11. CONTROLLING OFFICE NAME AND ADDRESS U.S. Department of Energy Washington, DC 20545	12. REPORT DATE March 30, 1982	
	13. NUMBER OF PAGES 48	
14. MONITORING AGENCY NAME & ADDRESS (if different from Controlling Office)	15. SECURITY CLASS. (of this report) UNCLASSIFIED	
	15a. DECLASSIFICATION/DOWNGRADING SCHEDULE	
16. DISTRIBUTION STATEMENT (of this Report)  Approved for public release; distribution unlimited.		
17. DISTRIBUTION STATEMENT (of the abstract entered in Block 20, if different from Report)		
18. SUPPLEMENTARY NOTES  *Present address: Mission Research Corporation, Alexandria, VA		
19. KEY WORDS (Continue on reverse side if necessary and identify by block number)		
Laser-plasma interaction	Ablation velocity	X-Ray backlighting
Double foils	Mass ablation rate	Tracer dots
Target velocity	Ablation pressure	Triple foils
Target velocity profiles	Pellet-shell velocity	Ablation plasma smoothing
20. ABSTRACT (Continue on reverse side if necessary and identify by block number)		
<p>→ Laser irradiated targets are ablatively accelerated to velocities near those required for fusion pellet implosions while remaining relatively cool and uniform. The target velocities and velocity profiles are measured using a double-foil method, which is described in detail. Also, the ablation plasma flow from the target surface is spatially resolved, and the scalings with absorbed irradiance of the ablation pressure, ablation velocity, and mass ablation rate are determined. Results are compared with hydrodynamic code calculations. ←</p>		

DD FORM 1473  
1 JAN 73

EDITION OF 1 NOV 65 IS OBSOLETE  
S/N 0102-014-6601

SECURITY CLASSIFICATION OF THIS PAGE (When Data Entered)



## ABLATIVE ACCELERATION OF PLANAR TARGETS TO HIGH VELOCITIES

### I. INTRODUCTION

One approach to inertial confinement fusion involves the use of a multಿನanosecond, moderate-irradiance laser pulse to implode a hollow pellet containing DT fuel.<sup>1</sup> If this concept is to succeed, the imploding pellet shell must be efficiently and uniformly accelerated to a high velocity, and the DT fuel must be kept cool. Only then will the pellet compress to densities sufficient for a high gain thermonuclear burn.

In this paper, we describe experiments which utilize ablatively accelerated planar targets to model large pellet shells early in the implosion phase. We have made detailed measurements of the motion of such targets<sup>2,3,4</sup> and of the ablation plasma that accelerates them.<sup>2,5,6</sup> These measurements include: emitted light studies, visible light shadowgraphy, and x-ray shadowgraphy on a novel target-impact foil (double-foil) configuration which is used to determine the mean velocities and velocity profiles of the dense part of the accelerated target, to study irradiance symmetrization, and to study double-foil interactions; diagnosis of the impact foil using a triple-foil configuration; spatially resolved studies of the ablation plasma flow from uniformly and nonuniformly irradiated targets; as well as measurements of the ablation plasma pressure, velocity, and mass ablation rate. The target velocity, velocity profiles, and the temperature of the target rear have been studied as a function of target thickness, irradiance, and irradiance uniformity. We have accelerated relatively cool and uniform targets to velocities of 160 km/sec - a velocity which is above the minimum thought to be required for laser fusion.<sup>1</sup> Our experimental results are compared to hydrodynamic code calculations.

Manuscript submitted January 6, 1982.

The experimental arrangement is described in Section II. Measurements on the accelerated target are described in Section III; and measurements of the ablation parameters are described in Section IV. Conclusions are offered in Section V.

## II. EXPERIMENTAL ARRANGEMENT

These experiments are performed using the NRL Pharos II Nd:glass laser ( $\lambda = 1.05\mu\text{m}$ ) which has been described elsewhere.<sup>7</sup> The laser beam is typically focused to a large diameter ( $\approx 1\text{mm}$ ) spot on the target surface by a 1.2 meter,  $f/6$  aspheric lens. Such large diameter, quasi-near field laser spots are used whenever possible to maximize irradiance uniformity and to minimize focal-spot-edge effects.<sup>2,5,8</sup> Irradiance profiles, such as those shown in Fig. 1, are measured on each shot in an equivalent target plane.<sup>9</sup> These profiles are fairly uniform with peak-to-valley variations of about  $\pm 35\%$ . Unless otherwise stated, irradiance is varied by adjusting the laser energy and not by changing the focal spot size. The laser pulse duration is 3-5 nsec FWHM.

Figure 2 shows the experimental arrangement. The target normal is tilted  $6^\circ$  from the laser axis to make it experimentally accessible. Surrounding the target are arrays of plasma calorimeters, in-situ calibrated ballistic pendula,<sup>2</sup> and time-of-flight ion collectors which monitor the ablation plasma and target energies, momenta, and velocities, respectively. (In this long pulse regime ion collector traces are narrow and single peaked, making them ideal for time-of-flight measurements.) From the angular distributions of these quantities we infer the ablation pressures, mass

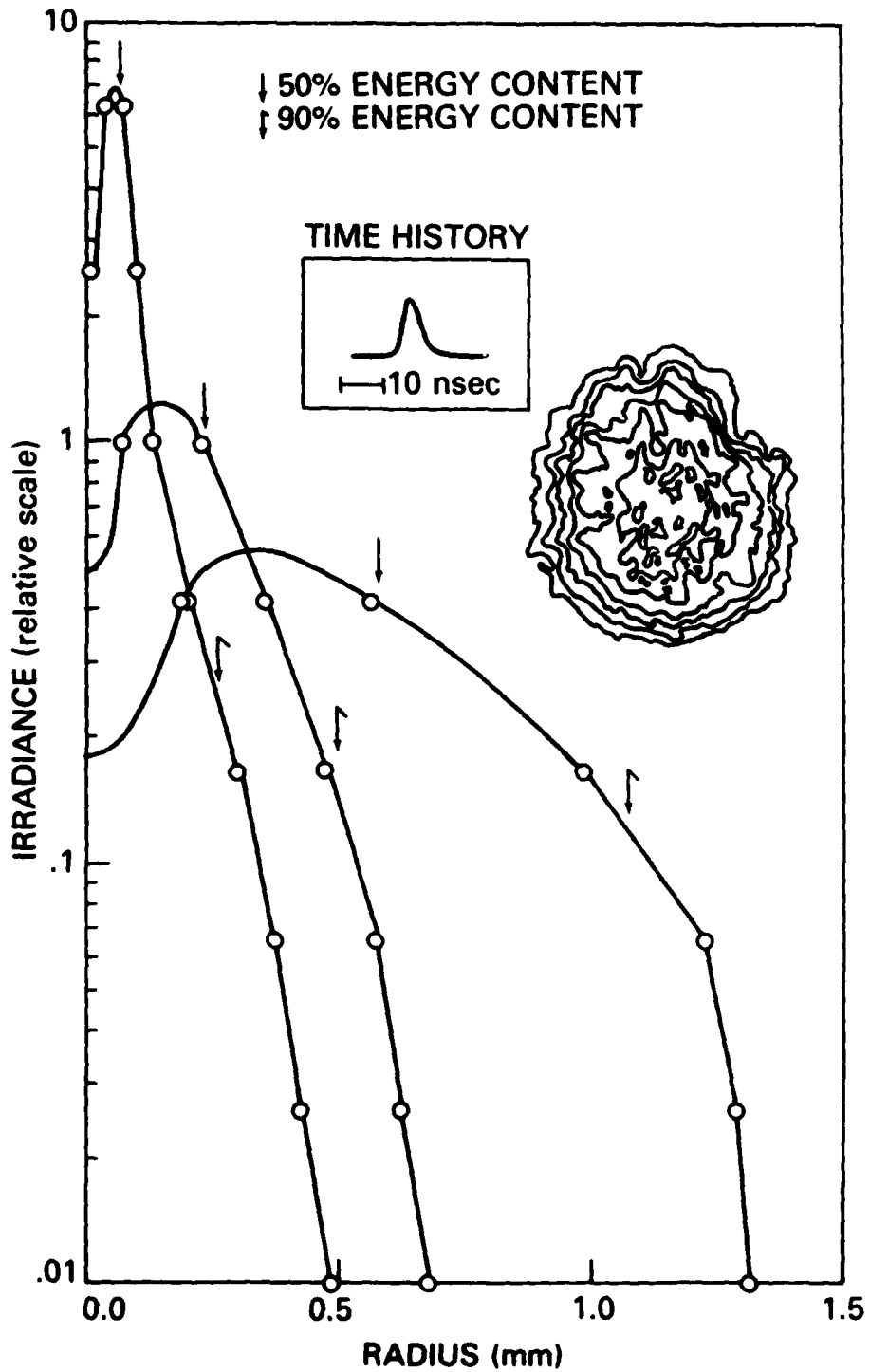


Fig. 1 - Azimuthally averaged radial intensity profiles at the target plane. Focal-spot radius is varied by moving the focusing lens. Arrows indicate radii within which 50% or 90% of the energy is contained. Inserts show the temporal behavior of the laser pulse and constant irradiance contours of a 1-mm diameter laser spot.

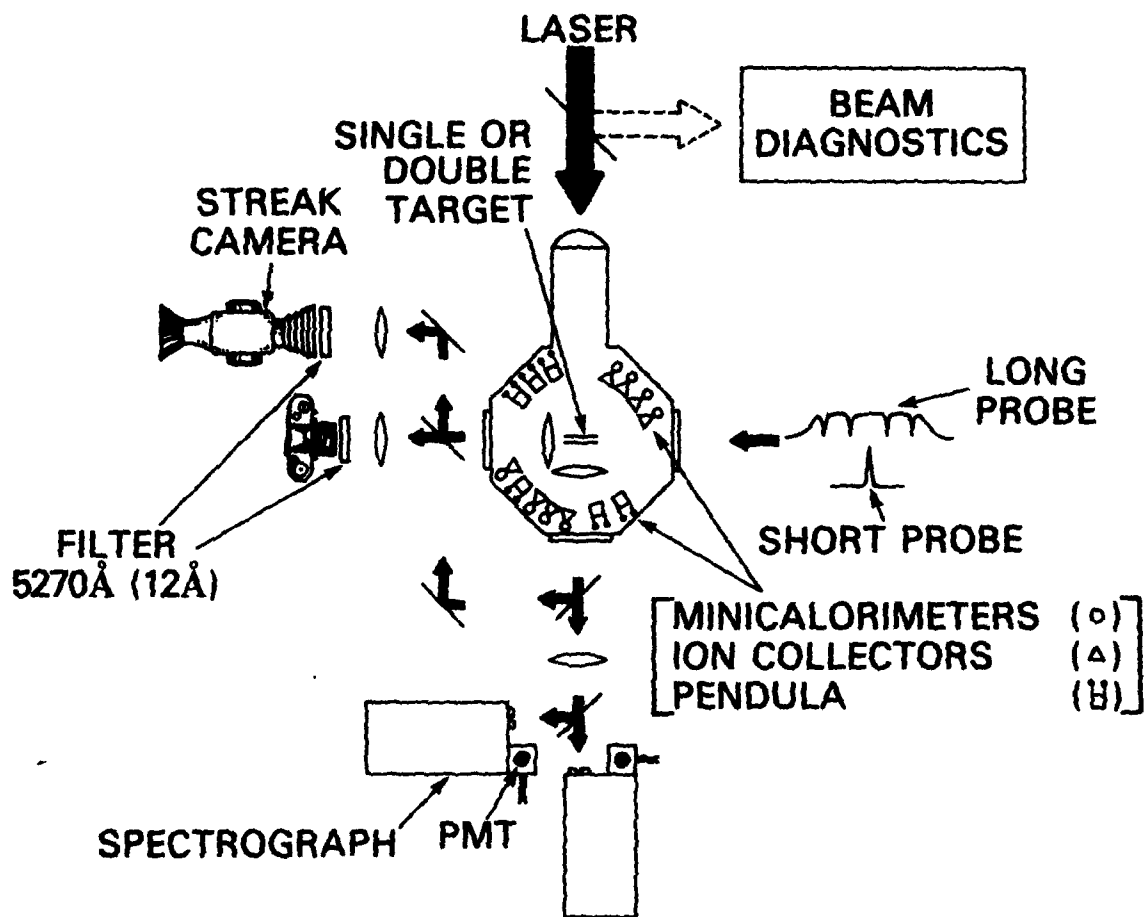


Fig. 2 - Sketch of the experimental setup

ablation rates, and ablation velocities. Although any two of the measured quantities are sufficient to calculate the third, we measure all three with independent diagnostics to verify the consistency and validity of the results. Spatially resolved pictures of the ablation plasma flow are also obtained using tracer elements deposited in the target surface.

Temporally and spatially resolved measurements of the target motion are made using a double-foil technique. This method consists of placing a thin foil (impact foil) behind the laser accelerated target and observing the reaction of the impact foil to its collision with the target (Fig. 3). We observe the two-foil interaction in three ways: (1) from the side with the optical shadowgraphy or optical streak arrangement shown in Fig. 2, (2) from the side using an x-ray backlighter, and (3) from the rear recording light emitted by the impact foil when it collides with the target. The details of particular double-foil configurations depend on the intent of the specific experiment and will be discussed in later sections.

Temporally resolved temperature at the rear surface of the accelerated target is determined by comparing the absolute visible continuum emission from the target's rear to black body emission.<sup>10</sup> The continuum intensity is measured at two different wavelengths using 3/4-m spectrographs coupled to 1-nsec risetime photomultipliers.

### III. TARGET BEHAVIOR

In earlier studies of ablative acceleration we inferred the target velocity from the velocity of its debris measured with time-of-flight ion collectors, and from the velocity of its optical shadow.<sup>8</sup> Each of these methods however, has limitations. Ion collectors, for example, measure

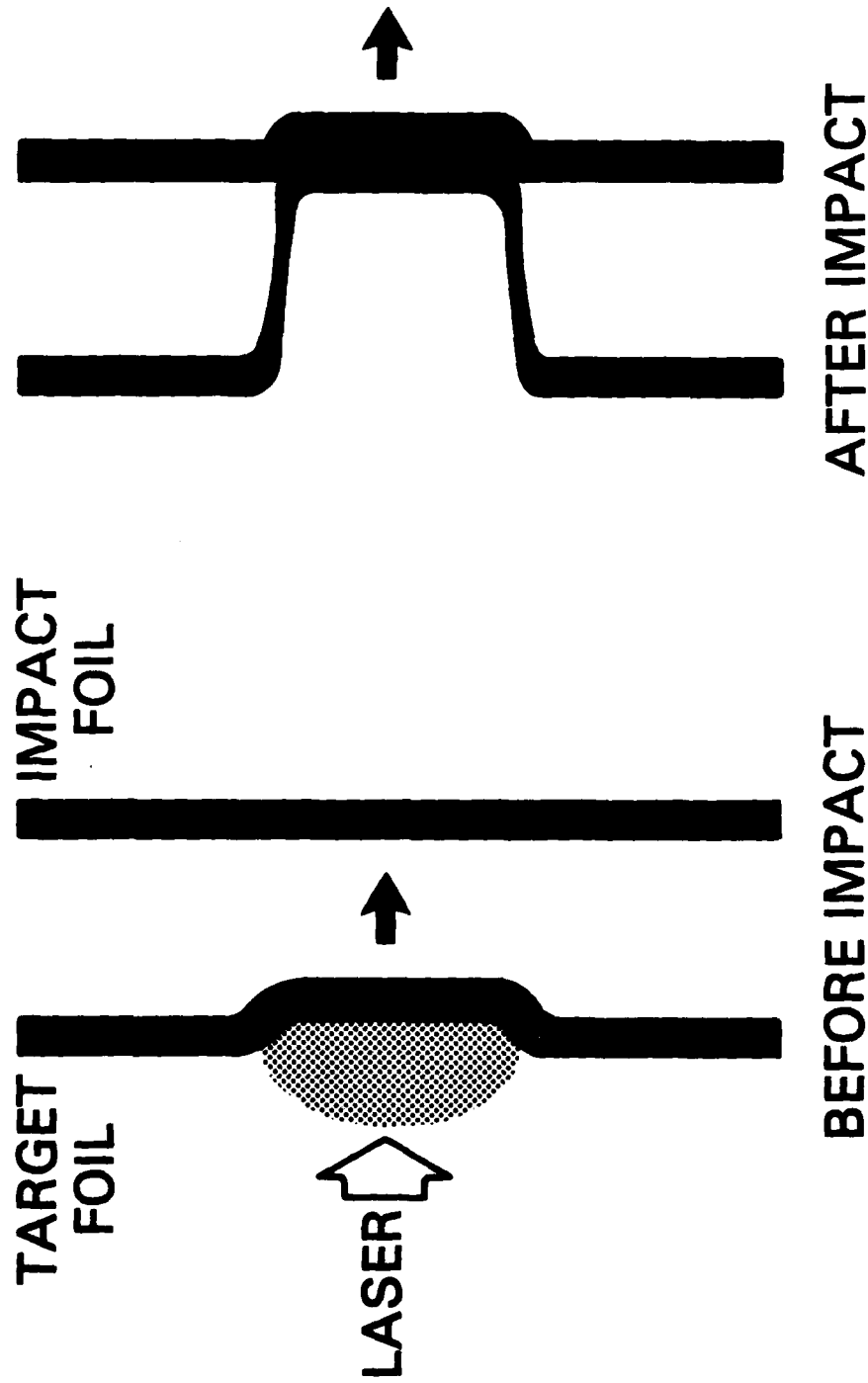


Fig. 3 — Schematic of the double-foil concept. Behavior of the laser accelerated target is inferred from the response of the impact foil to the collision.

properties of the target very far from its acceleration region, while optical shadowgraphs can not distinguish the high density part of the target from any low density plasma that may precede it. In the present work we use a double-foil technique<sup>11</sup> that discriminates against such a low density plasma, and permits temporally and spatially resolved diagnosis of the dense part of the target. Double foils may also be used to investigate hypervelocity impact phenomena such as the generation of ultra high pressures or to model double-shell fusion pellets.

With the double-foil method, the target velocity is determined from its flight time to the impact foil, placed a known distance away. The flight time, in turn, is determined by noting the moment at which the impact foil reacts to its collision with the target. Such reaction includes any of the observable phenomena normally associated with collisions - for example, spall or fluff from the rear of the impact foil, movement or deformation of the impact foil, or visible light emission from its rear surface. The target position as a function of time is measured by varying the initial target-impact foil spacing, thereby controlling the instant of collision. In this manner we can diagnose the target during as well as after its acceleration phase. Also, the visible light emission from the rear of the impact foil gives spatial resolution along the target surface so that the relationship between velocity and irradiance uniformity may be studied.

The choice of the target and impact-foil material, their dimensions, and the spacings between the two foils depend on the purpose of the experiment. To infer target velocities, for example, it is desirable that the impact foil be thin enough so that the sound-transit-time through it is very short

compared to the flight time of the target. In this case, the sound-transit-time may be ignored, and the collision time of the target with the front surface of the impact foil is directly related to the reaction of the impact foil's rear surface.

The ability of the double-foil method to discriminate against a low density plasma preceding the dense part of the target is demonstrated in Fig. 4. Here, we compare shadows cast by a single and a double-foil target that are temporally resolved by multiple-frame shadowgraphy using a 0.5 nsec, 5270-A laser probe flash. Both types of targets are photographed before, as well as 1.3 nsec, and 3.8 nsec after the peak of the laser pulse. Figures 4a, b, and c show shadowgraphs of the single target which is a  $7\text{-}\mu\text{m}$  thick CH foil. The shadow of this target moves with a velocity of  $1.6 \times 10^7$  cm/sec and traverses a distance of about  $400\mu\text{m}$  in 2.5 nsec. Figures 4d, e and f show a corresponding sequence for the double foil which is composed of a  $10\text{-}\mu\text{m}$  thick CH target and a  $7\text{-}\mu\text{m}$  thick aluminum impact foil. Note that although the target shadow has already reached the impact foil in Fig. 4e, the impact foil itself does not react at this time. In fact, the first indication of the impact foil's reaction occurs in Fig. 4f - more than 2.5 nsec after the optical shadow of the accelerated target reached the impact foil. Since the shock-transit-time through the impact foil is less than 1.4 nsec (sound speed in cold Al is  $5 \times 10^5$  cm/sec), much of this delay is caused by the material in the leading edge of the target shadow exerting insufficient pressure for the impact foil to react. Because the pressure exerted by a moving mass is proportional to its density, we conclude that the leading edge of the accelerated target shadow is composed of low density material. This low density material obscures the dense part of the

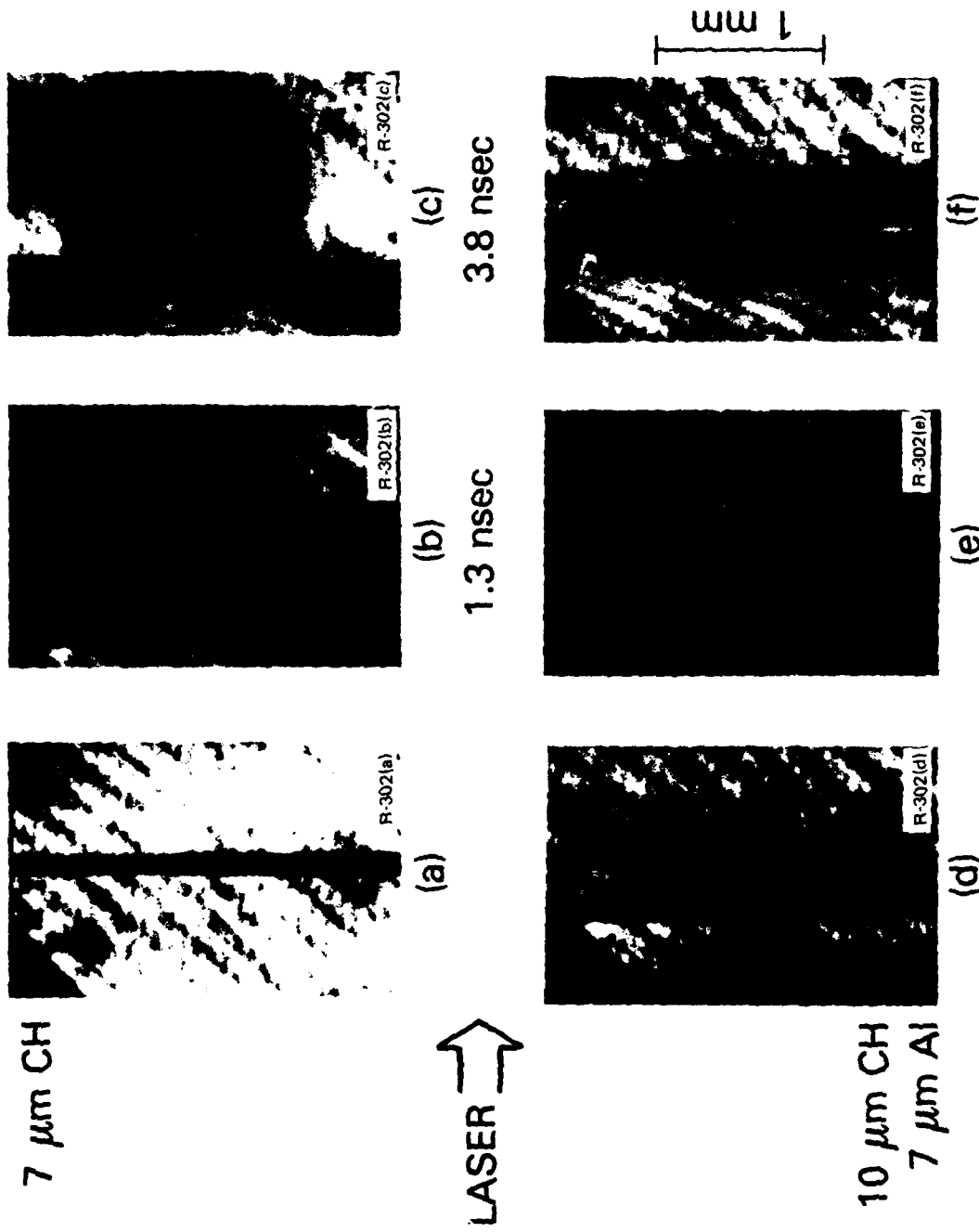


Fig. 4 - Optical shadowgraphs of single (a, b, c) and double-foil (d, e, f) targets irradiated at  $5 \times 10^{12}$  W/cm<sup>2</sup>. The times noted are relative to the peak of the laser pulse. Photographs b, c, and e, f are taken during the same shot.

accelerated target from optical shadowgraphy and interferometry diagnostics, but is discriminated against with the double-foil method.

Another way to view the delayed reaction of the impact foil is presented in Fig. 5, which shows the streak record of a double-foil collision backlit by a 10-nsec, 5270-Å laser probe. This one-dimensional, but temporally continuous, shadowgraph shows the low density plasma advancing toward the impact foil, the low density plasma-impact foil collision, and the reaction of the impact foil when the dense part of the accelerated target finally strikes. The sudden reaction time ( $\approx 0.5$  nsec) of the impact foil suggests a localized, dense accelerated target. The time of the dense target - impact foil collision is, therefore, a good marker for the target time-of-flight.

We determine a target velocity by varying the initial target - impact foil separation and accumulating distance traveled versus time-of-travel data for many shots. Such data for 7- $\mu\text{m}$  thick and 10- $\mu\text{m}$  thick CH targets irradiated at  $6 \times 10^{12}$  W/cm<sup>2</sup> are shown in Fig. 6. For most of these cases, the target-impact foil separation is large enough so that the collision occurs after the ablative acceleration phase is nearly over. Therefore, the data for each target thickness lie on a straight line whose slope is the final target velocity. Velocities obtained in this way agree with predictions based upon measurements of the ablation momentum (pressure), mass ablation rate (section IV) and momentum conservation, and with the predictions of a hydrodynamic code described below. However, they are significantly lower than the low density plasma velocities inferred from the motion of the target's optical shadow in the double-foil streak pictures. Averaged over many shots, the ratio of the optical shadow velocity to

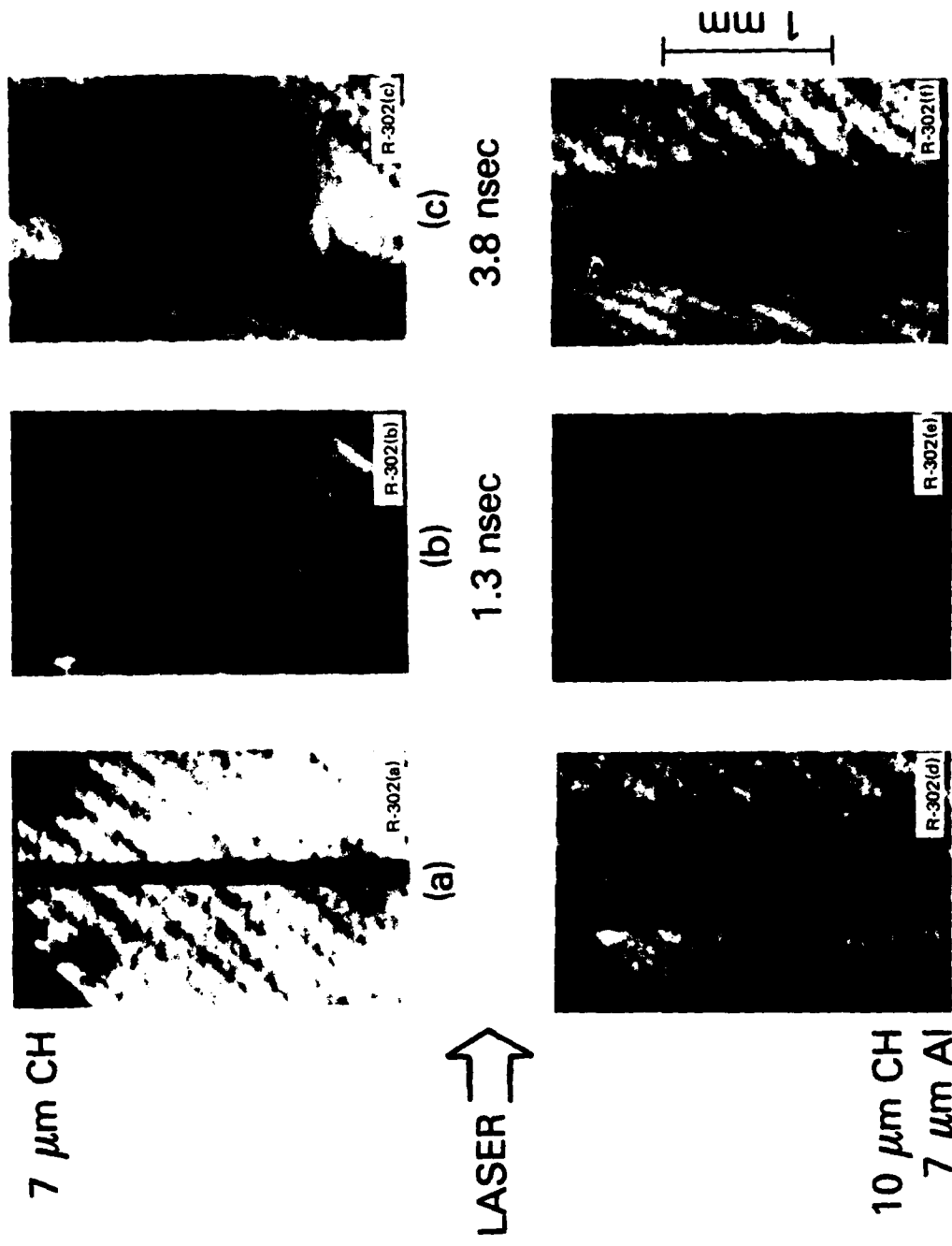


Fig. 4 - Optical shadowgraphs of single (a, b, c) and double-foil (d, e, f) targets irradiated at  $5 \times 10^{12}$  W/cm<sup>2</sup>. The times noted are relative to the peak of the laser pulse. Photographs b, c, and e, f are taken during the same shot.

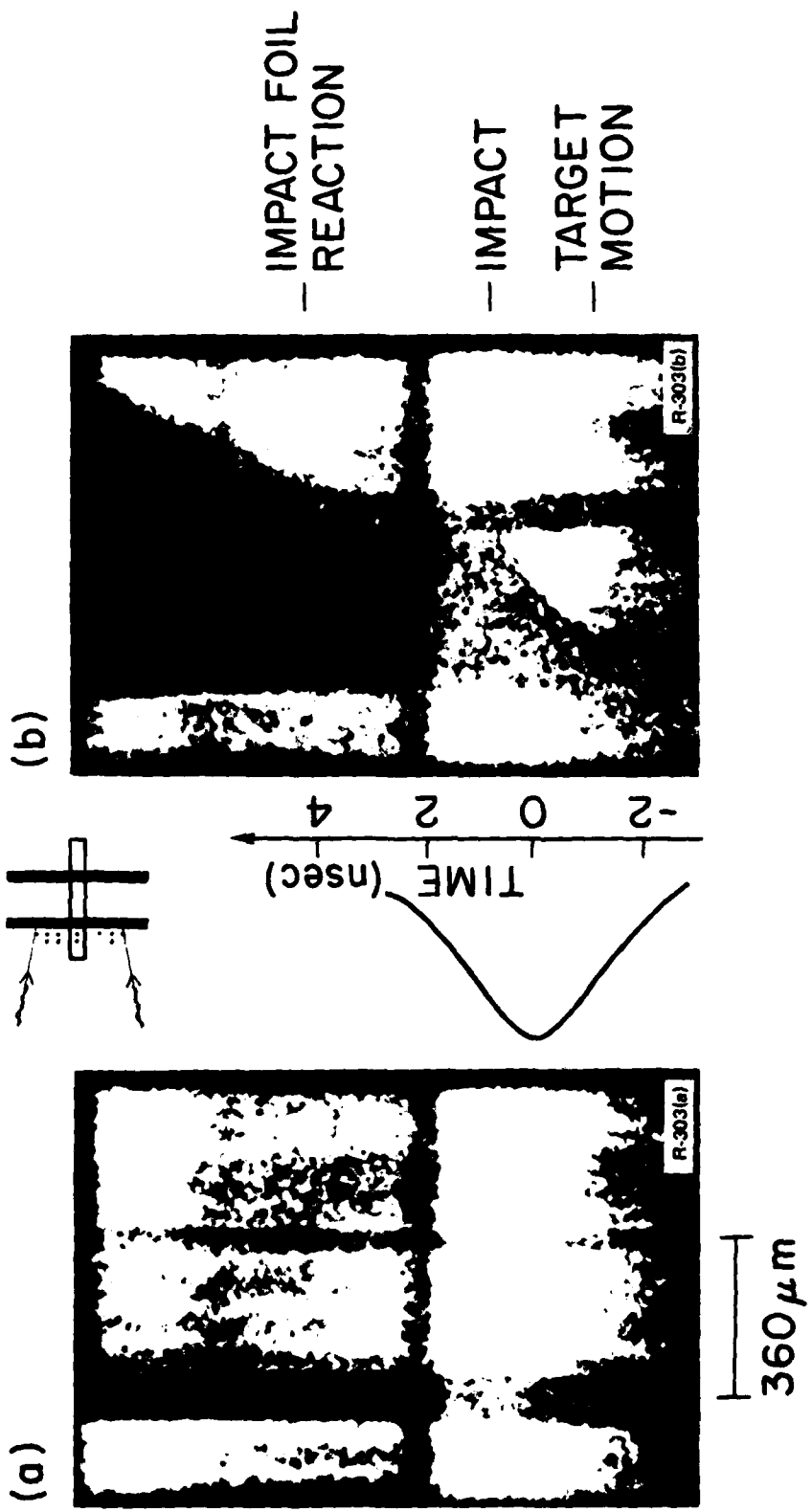


Fig. 5 - Streaked optical shadows of a target colliding with an impact foil: (a) - before shot, and (b) - after shot. The target is 7- $\mu$ m thick CH and the impact foil is 7- $\mu$ m thick Al.

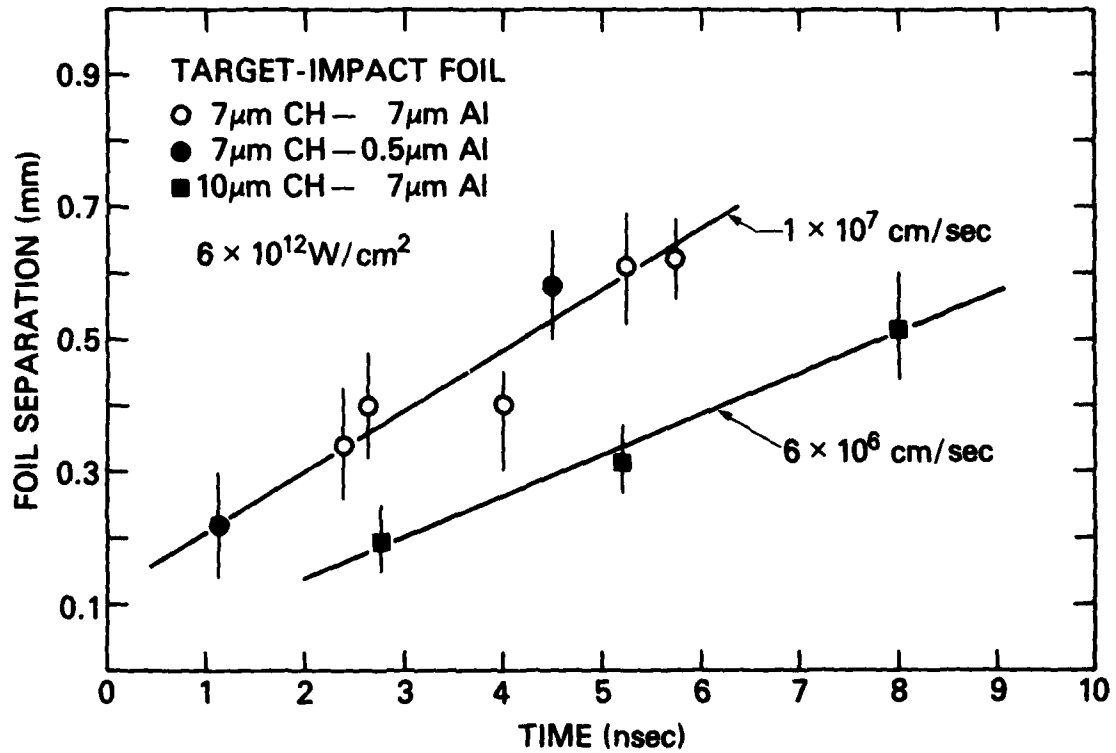


Fig. 6 - A graph of target-impact foil separation versus the time (with respect to an arbitrary origin) at which the impact foil reacts to its collision with the target. The slopes of lines drawn through points accumulated over many shots give the dense target velocities. The laser pulse duration is 4-nsec FWHM.

dense target velocity is  $2 \pm 0.8$ , with the spread mostly due to shot-to-shot variations in the low density plasma velocity. This ratio is consistent with the leading edge of the low density plasma being caused by spall or fluff from the unloading of a shock at the target's rear surface.

The phenomenon of a low-density, rear-surface plasma is not restricted to the laser accelerated target. Thus, the acceleration of the impact foil obtained using optical probe light (Fig. 5) cannot be used to infer the pressure history in the collision because like the target shadow, the impact-foil shadow is also cast by low density material and not by the dense part of the impact foil. This is demonstrated in Fig. 7 where the behavior of the impact foil is diagnosed using a third foil.

Backlighting the double foils with x rays provides a way to directly measure the motion of the dense portion of both foils. An x-ray shadowgraph of a double foil photographed using a  $\frac{1}{2}$ -nsec duration Al x-ray flash ( $\approx 1.6$  keV) as a backlighting source, is shown in Fig. 8.<sup>4</sup> This figure is the x-ray shadowgraph of a  $7\text{-}\mu\text{m}$  thick carbon target irradiated with  $3.5 \times 10^{12}$  W/cm<sup>2</sup>, and moving at  $3\text{-}4 \times 10^6$  cm/sec before its collision with a  $7\text{-}\mu\text{m}$  thick carbon impact foil. The shadows visible in Fig. 8 are the unaccelerated foil, the accelerated target, and the impact foil. Bright regions are due to the x-ray flash and x-ray emission from the plasma corona on the target's front surface. We estimate, from x-ray absorption data in cold carbon and the observed path lengths, that the shadows are caused by material that is at least 3% of solid density. Thus, the figure shows that the dense, accelerated target traversed most of the distance to the impact foil - a distance 30 times its thickness - without noticeable breakup. It is evident too that the impact foil does not react appreciably

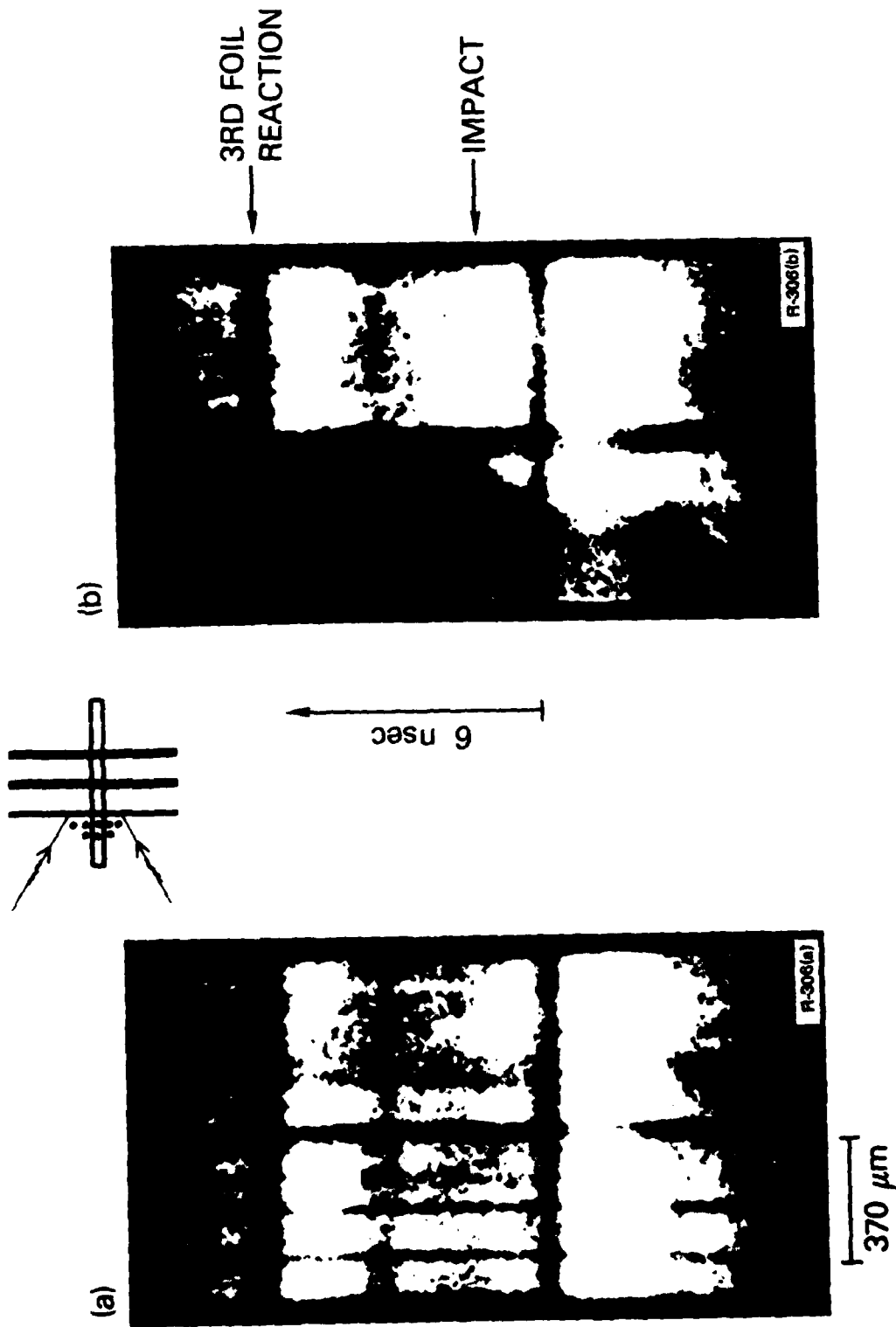


Fig. 7 - Triple-foil experiment: A third foil diagnoses the second foil. The laser accelerated target is  $3\text{-}\mu\text{m}$  thick C and the two impact foils are  $7\text{-}\mu\text{m}$  thick C respectively.

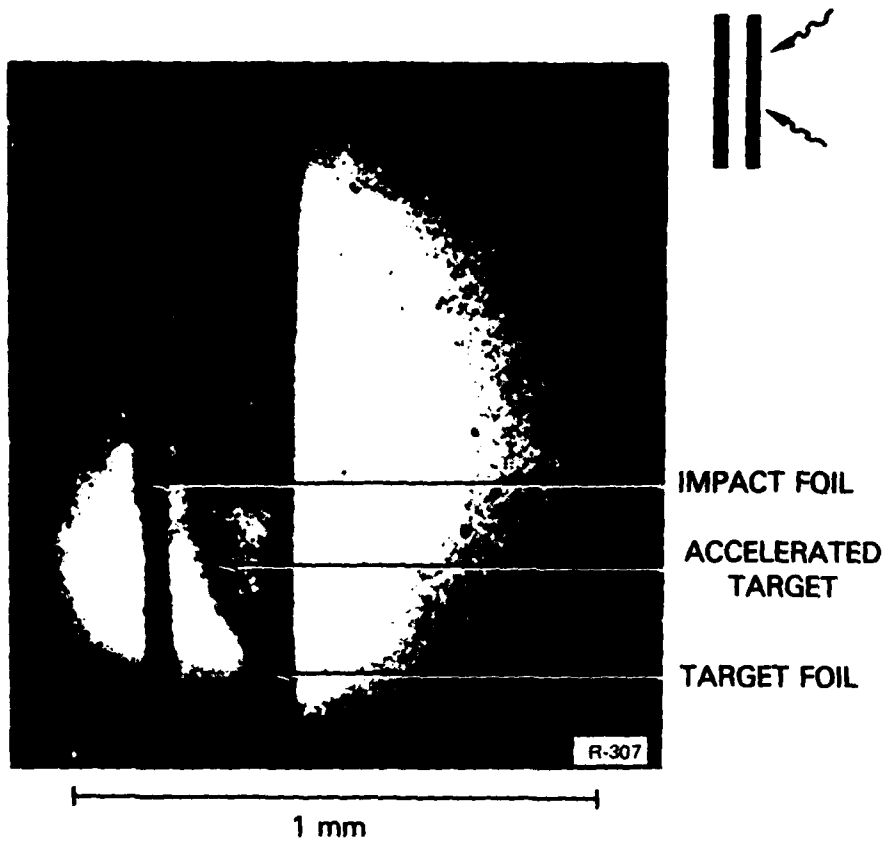


Fig. 8 — X-ray shadowgraph of a double foil before the target-impact foil collision. The x-ray flash is  $\frac{1}{2}$  nsec long and occurs 5 nsec after the peak of the laser pulse. Pinhole smearing and time smearing are about  $20\mu\text{m}$  each.

before it is hit by the high density part of the target. These observations support our interpretation of results from the double-foil method. Also, velocities obtained by x-ray backlighting agree with those obtained by the double-foil method: velocities obtained with the two methods, on different shots, are the same to within 35%.

It is also interesting to note that the accelerated target is not "cut out" from the rest of the target foil, but is connected to it with a near solid density bridge. The gap between the accelerated target and the target foil is thus effectively closed so that front surface plasma cannot flow to the impact foil and disturb our measurements. This bridge, in addition, prevents front surface plasma from heating the rear of the target, and thereby spuriously increasing the rear surface temperatures measured in reference 10 and later in this paper.

We have computed target velocities and density profiles using a one-dimensional fluid code that has been described elsewhere.<sup>12</sup> This code utilizes a sliding zone Eulerian grid with flux corrected transport (FCT). The physics included in the code are: a single temperature fluid, classical transport physics with Spitzer heat conduction, and the same temporal irradiance history as the experiment. Absorption is by inverse bremsstrahlung in the underdense region with any remaining energy dumped smoothly into two zones surrounding the critical surface. The only target preheating considered is by shocks. Examples of computed density profiles for thin, fast targets and thick, slow targets are shown in Fig. 9. Both the thick and thin target in the figure are compressed during the acceleration phase. Afterwards they expand somewhat and develop a low density foot that precedes the dense target. Such a low density foot in front of the dense target material is

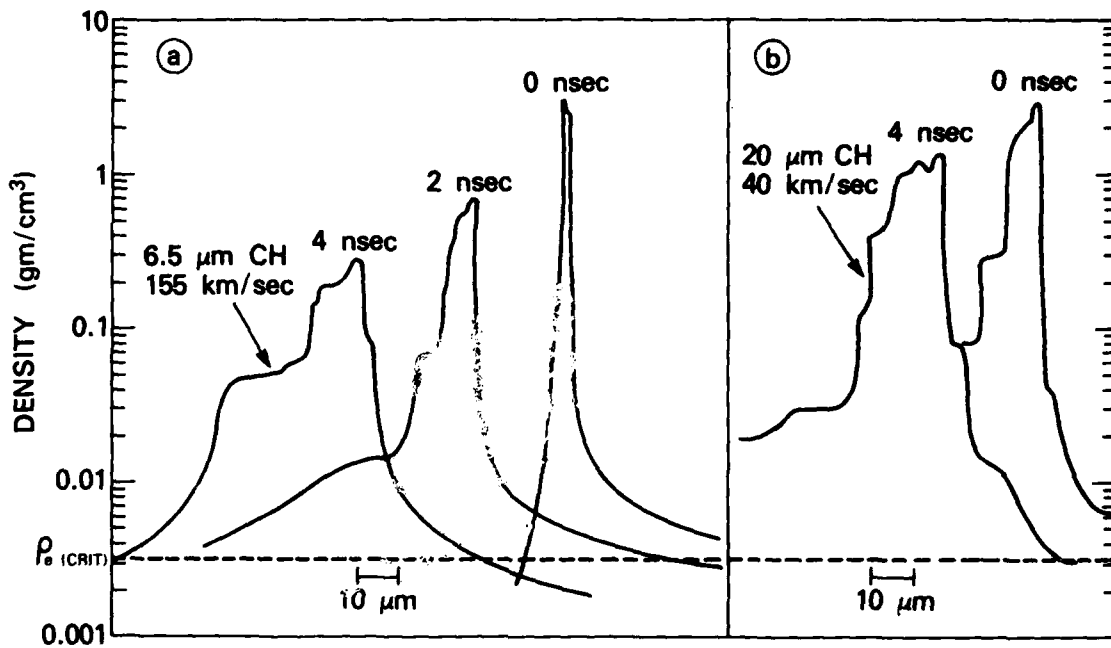


Fig. 9 — Density profiles of a thin and a thick target accelerated to high velocities. The laser is incident from the right;  $\rho_{e(crit)}$  is the critical electron density. The simulation conditions are: (a)  $1.6 \times 10^{13}$  W/cm<sup>2</sup> absorbed, 2.6-nsec pulse duration, 6.5- $\mu$ m thick CH target and (b)  $1 \times 10^{13}$  W/cm<sup>2</sup> absorbed, 4-nsec pulse duration and 20- $\mu$ m thick CH target.

inferred in the experiment. The expansion rate of the dense target is much smaller than its directed velocity. However, the expansion rate and the length of the low density foot are probably underestimated in the calculation because preheat mechanisms other than shock heating are not included.

In addition to measuring target velocity magnitude, measuring the target velocity profile across the target is also important. This is because nonuniformly accelerated pellet shells will not achieve high compression ratios and will thereby degrade the pellet gain. Nonuniform target velocities could arise from any number of sources such as hydrodynamic instabilities, nonuniform targets or nonuniform irradiation. We now address the third issue, namely: Are target velocity profiles and irradiance profiles directly related, or will a mechanism such as thermal conduction in the ablation plasma smooth irradiance nonuniformities? Answers to this question will influence the choice and design of lasers for direct illumination pellet implosions.

To measure target velocity profiles we utilize the visible light which is emitted from the rear surface of the impact foil during its collision with the target. The time of this emission corresponds closely to the time of the dense target-impact foil collision as determined from double-foil streak shadowgraphy (Fig. 10), making the emission a good time marker from which the target velocity may be derived. Now, if a nonuniformly accelerated target collides with an impact foil the regions of the impact foil struck by fast portions of the target will emit first. Conversely, the regions of the impact foil struck by slower portions of the target will emit later. Consequently, target velocity profiles may be determined from differences in emission time

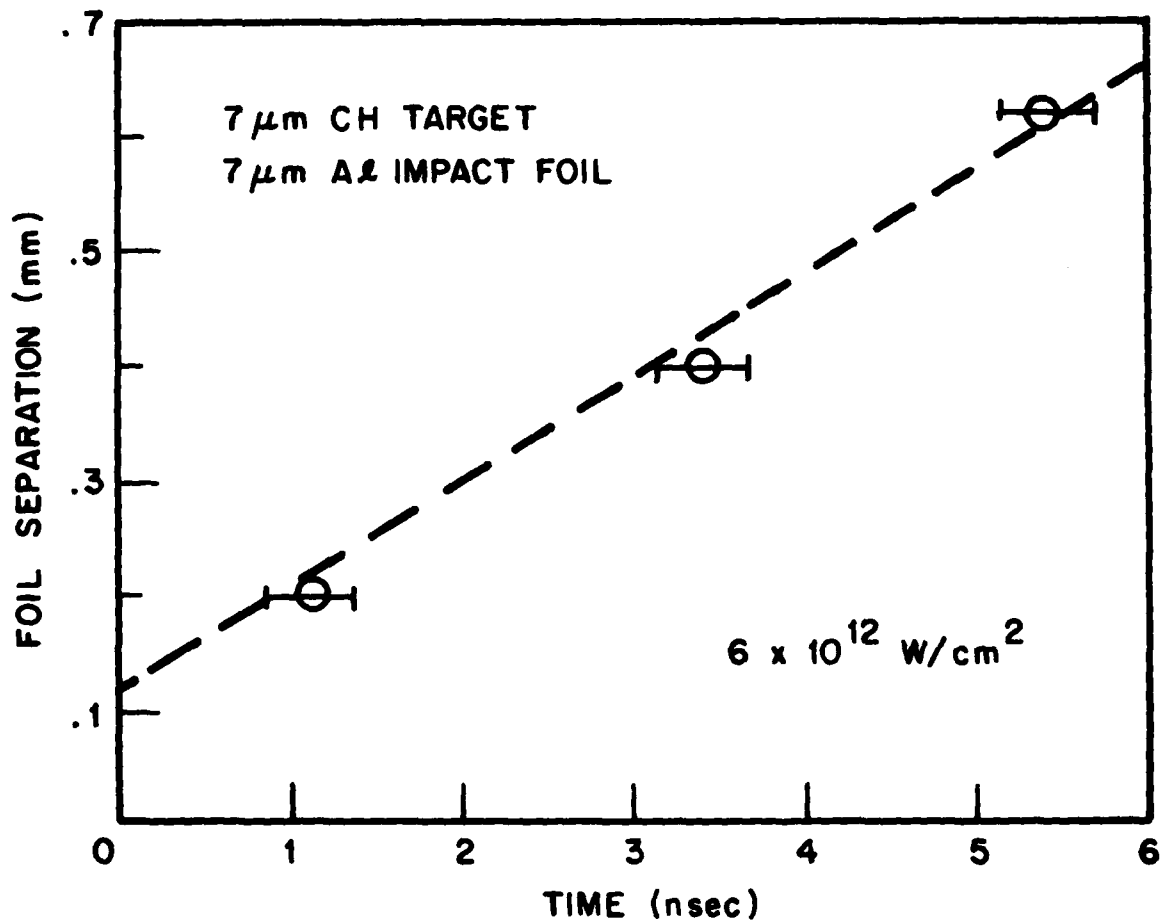


Fig. 10 - Foil separation versus collision time determined in two ways: 1) from double-foil streak shadowgraphy (dashed line), and 2) from light emission at the rear of the impact foil (O). Light emission is measured at 10% of the full scale reading of the spectrograph photomultiplier.

across the impact foil's surface.

The relationship between a dense target-impact foil collision and the visible emission from the impact foil's rear surface is graphically illustrated by Figs. 11a and 11b. Figure 11a shows the x-ray shadowgraph of an impact foil after it has collided with a nonuniformly accelerated target. Nonuniform acceleration was purposefully induced by a laser pulse whose spatial intensity profile was distorted with a rectangular mask that blocked a portion of the laser beam thus casting a low-intensity shadow across the center of the focal spot. Under these conditions, the directly irradiated regions of the target accelerate ahead of the shadowed region and subsequently impress their shape on the impact foil. Streaked emission from the rear of an impact foil struck by a nonuniformly accelerated target is shown in Fig. 11b. In this figure, we used a double-foil configuration in which the impact foil was transparent so that emission from the accelerating target rear and the impact foil rear could be recorded on the same shot. The temporal history of this emission is as follows. Before the collision, and while the impact foil is transparent, only the emission from the target is seen. This emission emanates initially only from those target regions that are directly irradiated - as seen on the left of Fig. 11b. As time goes on, however, the emitting region spreads in space causing both the directly irradiated and shaded target regions to appear luminous. Such spread may be caused in part by the expansion of the low density, luminous plasma that precedes the dense part of the target and, perhaps, in part by shock heating of the shaded region of the target. Whatever the mechanism, when the low density portion of the target reaches the impact foil, the foil's optical opacity

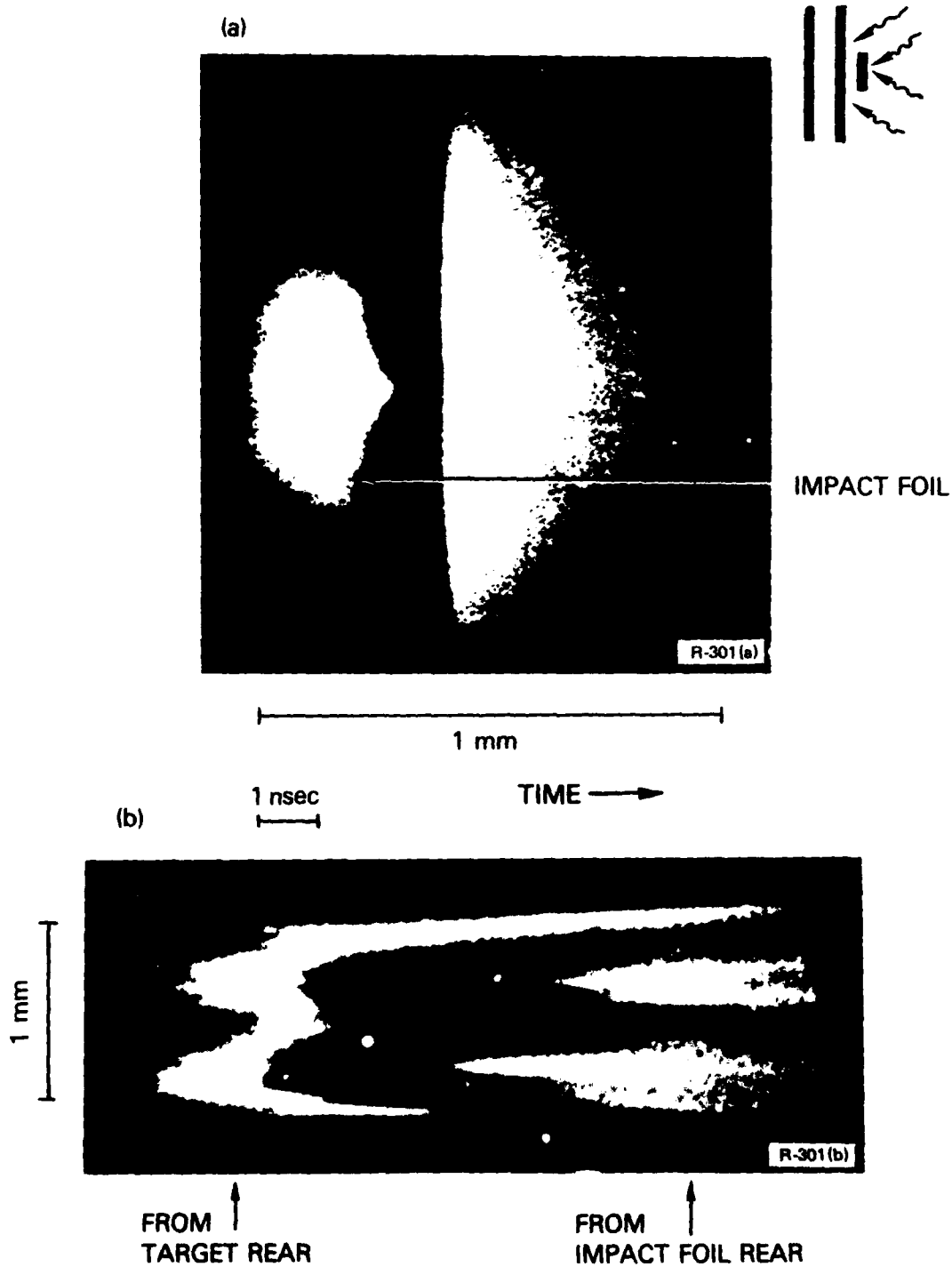


Fig. 11 - (a) X-ray shadowgraph of the collision between a nonuniformly accelerated target and an impact foil. This picture was taken after the target and the impact foil collided. X-ray flash and pinhole smearing conditions are the same as in Fig. 8. (b) Visible emission from the rear of a nonuniformly accelerated target and from the rear of an impact foil struck by that target.

is increased so that the target emission is no longer visible, and the middle of the streak record appears dark.<sup>13</sup> Afterwards, when the high density portion of the target finally collides with the impact foil, the impact foil's rear begins to emit from two well defined lobes. These luminous lobes correspond to the two impact foil bulges in Fig. 11a. Thus, we have further evidence that emission from the impact-foil rear is sensitive to velocity nonuniformities in the dense portion of the target. Target structure which may be obscured from direct view by a low density plasma is unmasked by the double-foil method.

The speed of the light emission front propagating through aluminum impact foils has been directly measured by using impact foils with a thickness step on their rear surface and noting the time difference between emission from the two sides of the step. We found that the emission front was supersonic ( $10^6$  cm/sec) when the foils collided during the laser pulse, i.e., when the target was still accelerating; but it was close to sonic if the collision occurred after the acceleration. The supersonic velocities are consistent with shock heating causing the rear-surface light emission. The lower, sonic velocities can be explained by assuming that decompression of the target after acceleration cushions the collision impact preventing the formation of a strong shock. Nevertheless, mechanisms other than shock heating cannot be excluded.

Figure 12a shows the velocity profiles of dense targets accelerated to 160 km/sec - a velocity above the lower limit thought to be required for laser fusion.<sup>1</sup> The rear-surface brightness temperature of these targets is measured to be below 10eV throughout the acceleration (Fig. 12b). Their speed is consistent with the predictions of our hydrodynamic code. The code,

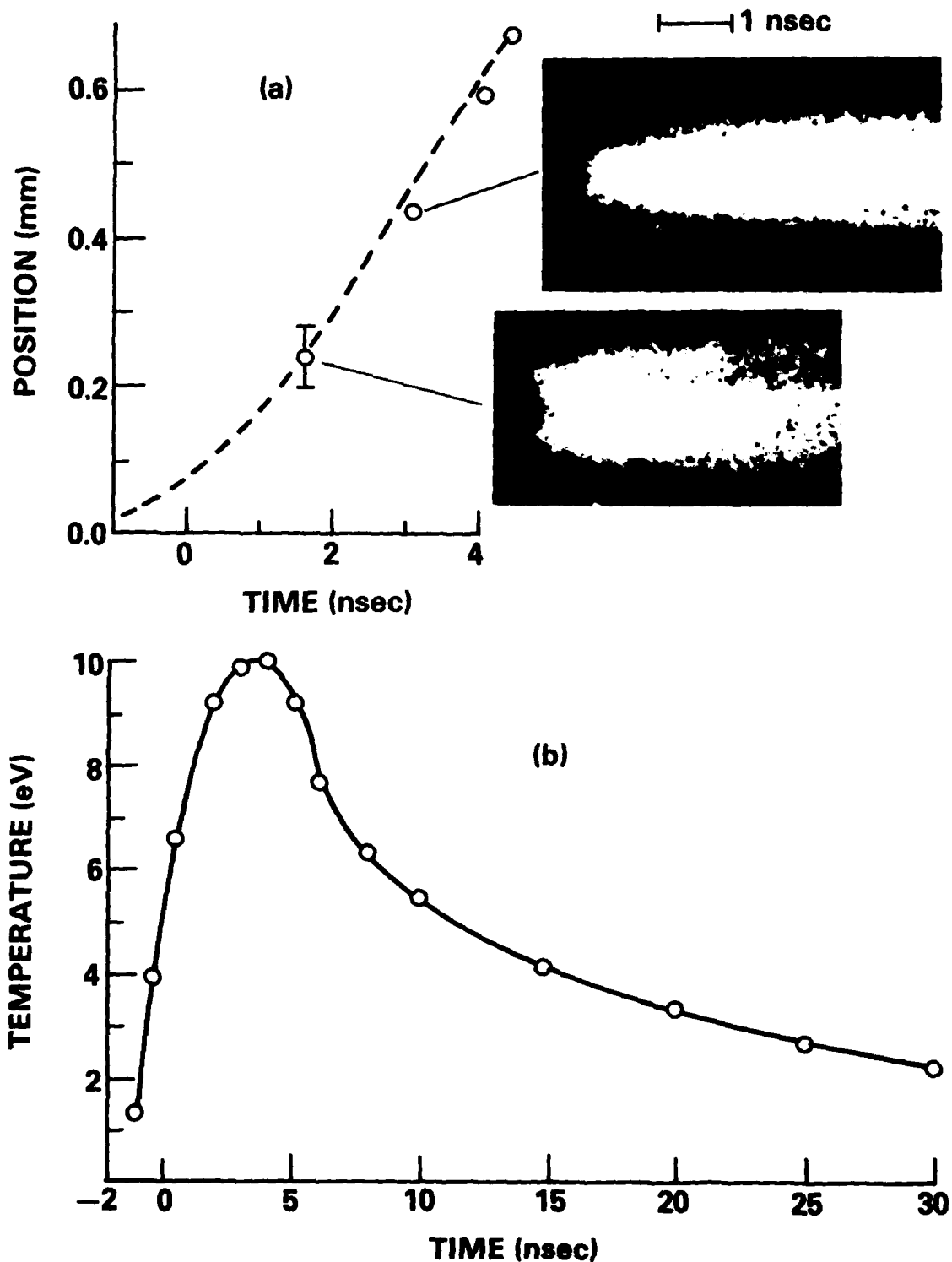


Fig. 12 - (a) Velocity profiles and measured positions (0) of CH targets accelerated to 160 km/sec. The dashed line (- - -) is a theoretical fit based on the ablation pressure and mass ablation rate scaling laws described in Section IV. The targets are  $6.5\mu\text{m}$  thick, the laser pulse length is 2.6 nsec, the laser-spot diameter is  $600\mu\text{m}$ , and the incident irradiance is  $2.9 \times 10^{13} \text{ W/cm}^2$ . Velocity profiles are measured with the double-foil method. (b) Rear surface temperature of these targets versus time. The peak of the laser pulse occurs at 0 nsec.

for example, predicts the measured target velocities at an absorbed irradiance of  $1.6 \times 10^{13}$  W/cm<sup>2</sup> (Fig. 9a), while the experiment utilizes an incident irradiance of  $2.9 \times 10^{13}$  W/cm<sup>2</sup> which - with 80% absorption<sup>8</sup> - is equivalent to an absorbed irradiance of  $2.3 \times 10^{13}$  W/cm<sup>2</sup>. Focal-spot-edge effects<sup>2,5,8</sup> at the relatively high irradiance and small laser spot size of this measurement (600  $\mu$ m diameter) probably reduce the effective irradiance below  $2.3 \times 10^{13}$  W/cm<sup>2</sup> and bring it closer to the predicted value.

The fast moving targets in Fig. 12a exhibit a velocity nonuniformity  $(V_{\max} - V_{\min})/V_{\min}$  of only 15%, even though the peak-to-valley nonuniformities of our laser beam are about 2 to 1 (Fig. 1). This smoothing of laser nonuniformities may be due to the so-called "cloudy day effect"<sup>14</sup> in which laser radiation absorbed near the critical surface is thermally smoothed by the time it is transported to the ablation surface, where most of the pressure is applied to the target. We did, in fact, make measurements on the ablation plasma which qualitatively support such a mechanism. These measurements will be shown at the end of Section IV.

We have also conducted quantitative studies of the relationship between laser nonuniformities and target velocity nonuniformities.<sup>3</sup> To simplify the analysis we used slowly moving foils accelerated to no more than 50 km/sec. Under these conditions, the fraction of mass ablated from these foils is small so the velocity nonuniformities are expected to scale almost linearly with irradiance nonuniformities in the absence of smoothing, i.e.,

$(V_{\max}/V_{\min}) \propto P_{\max}/P_{\min} \propto (I_{\max}/I_{\min})^{.8}$ , where the scaling of pressure with irradiance derived in Section IV is used. Velocity nonuniformities below this scaling indicate the presence of a smoothing mechanism.

Some velocity nonuniformity results are shown in Fig. 13. Figures 13a and b show the emission from impact foils struck by targets irradiated with

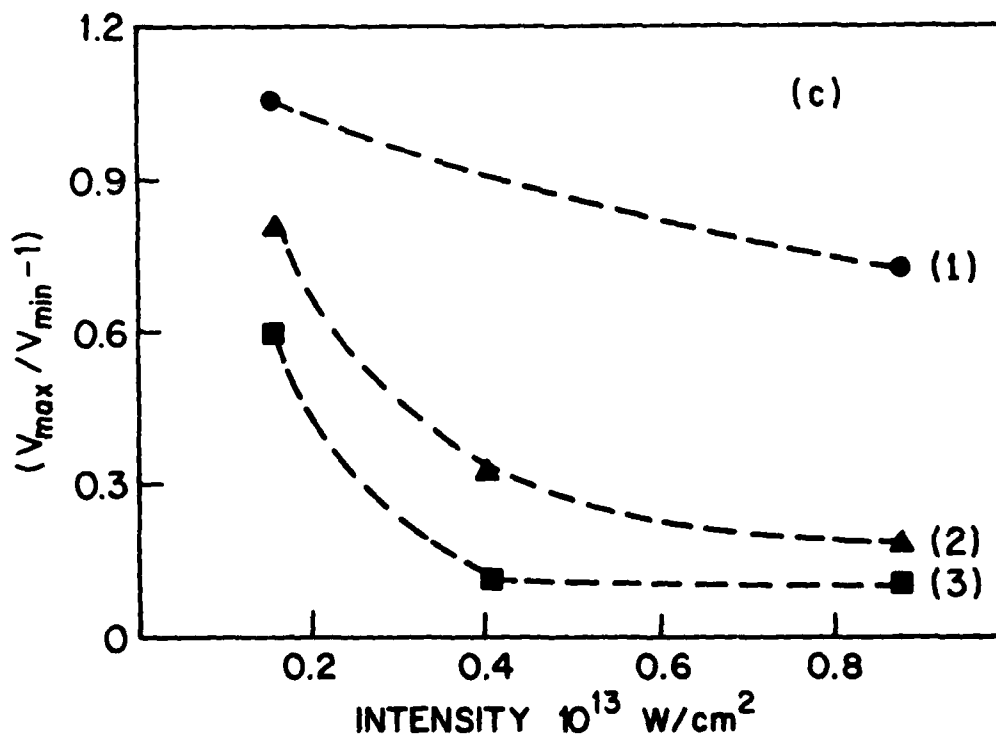
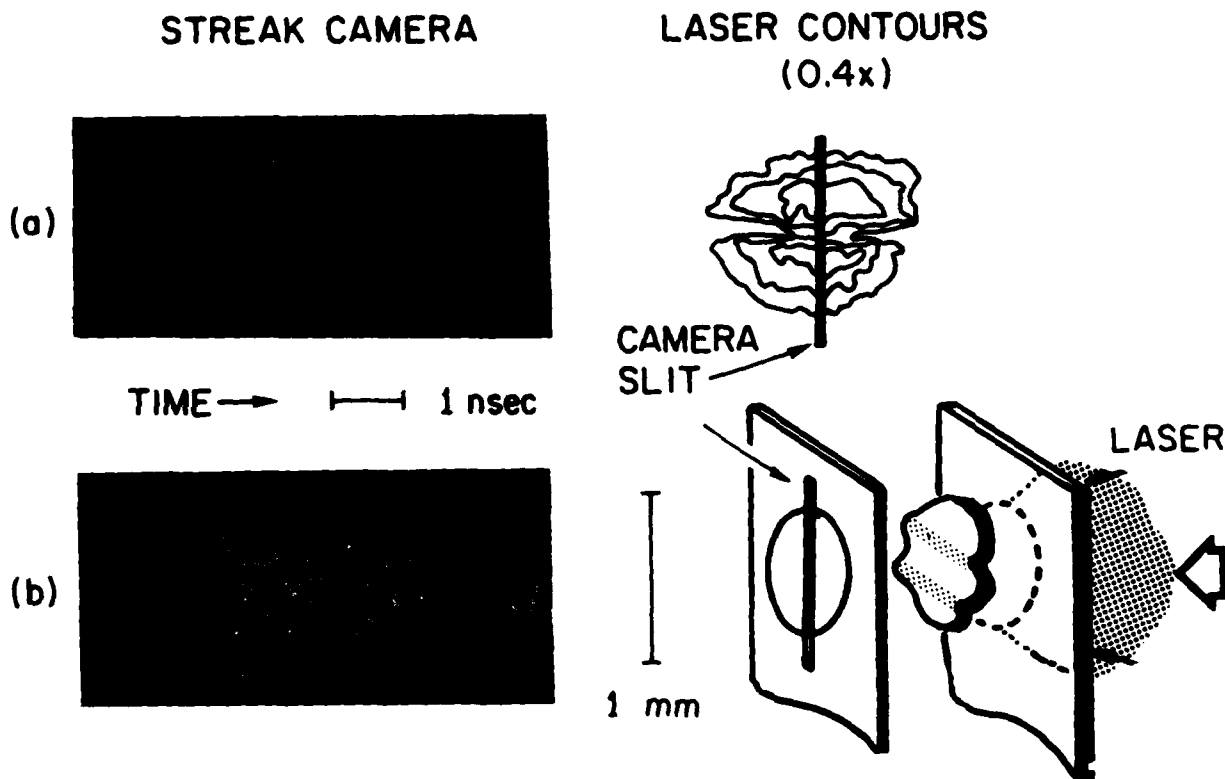


Fig. 13 - (a), (b) Streak records of emission from the rear surface of an impact foil struck by a target irradiated with a structured laser profile. The mean irradiances are (a)  $4 \times 10^{12} \text{ W/cm}^2$  and (b)  $9 \times 10^{12} \text{ W/cm}^2$ . (c) Target velocity nonuniformities graphed as functions of average irradiance for different dips in the incident beam: (1)  $I_{\max}/I_{\min} \approx 10$ , 220- $\mu\text{m}$  FWHM dip; (2)  $I_{\max}/I_{\min} \approx 6$ , 140- $\mu\text{m}$  FWHM dip. (3)  $I_{\max}/I_{\min} \approx 2$ , 140- $\mu\text{m}$  FWHM dip. Case (2) has the laser focal-spot contours shown in the figure.

the spatially structured laser beam shown in the inset at two different average irradiances. Note how the velocity nonuniformities are markedly reduced at the higher irradiance! Calculations<sup>12</sup> indicate that in this irradiance regime the ablation to critical surface separation increases with irradiance as  $I^{0.7}$  and is about  $100\mu\text{m}$  at  $10^{13}\text{ W/cm}^2$ . Therefore, these results are qualitatively consistent with a thermal conduction mechanism which smoothes laser nonuniformities when the ablation surface to critical surface distance is comparable to the nonuniformity scalelength.

Figure 13c shows measurements of velocity nonuniformity versus average irradiance for several laser irradiance profiles. In all cases there is an increase of irradiance profile smoothing with higher average irradiance. At the highest irradiance studied,  $140\text{-}\mu\text{m}$  FWHM dips in intensity are almost completely smoothed out but the  $200\text{-}\mu\text{m}$  FWHM dips in intensity are imprinted on the target. This again is qualitatively consistent with thermal smoothing over the ablation to critical distance predicted at this irradiance. It remains to be seen whether larger wavelength perturbations at somewhat higher irradiances are similarly smoothed out. If they are, then the 1-3% ablation pressure uniformities required for a high-gain pellet<sup>15</sup> may be achievable with realistic laser systems.

#### IV. ABLATION PLASMA STUDIES

In this section we present measurements of ablation plasma properties relevant for the target velocity measurements described in the last section. Also, using a tracer technique to spatially resolve the ablation plasma flow, we provide evidence that the observed smoothing of target velocity profiles is indeed caused by smoothing in the ablating plasma.

Both foils and disk targets are chosen for these studies. Each type

of target has its own advantage: Wide foils, for example, do not permit ablation plasma to flow around the foil edge and interfere with rear surface measurements. Disk targets, on the other hand, can be irradiated relatively uniformly by using a focal-spot diameter larger than the disk diameter, and, since the laser-target interaction area  $A$  is fixed by the finite geometry, average irradiances as well as ablation pressures ( $\propto$  momentum/area) and mass ablation rates ( $\propto$  mass/area) may be reliably calculated. Also, any energy that escapes the interaction area is easily detected and its effect on the results easily estimated. A small amount of ablation plasma energy has indeed been measured at the rear of disk targets with plasma calorimeters, but its effect is minimal in our experiments. For example, for 300- $\mu\text{m}$  and 600- $\mu\text{m}$  diameter disks less than 20% of the total absorbed (plasma and target) energy is detected at the rear of the disk, while for 1000- $\mu\text{m}$  and 1200- $\mu\text{m}$  diameter disks less than 5% of the absorbed energy flows rearward. At the irradiances employed in these experiments, this excess energy is probably due to the flow of hot thermal plasma around the disk edges. Very energetic suprathreshold electrons observed in  $\text{CO}_2$  laser experiments<sup>16</sup> and at higher irradiance Nd laser experiments<sup>17</sup> are not the dominant mechanism here, as evidenced by the low level of x-ray emission observed above 20 keV.<sup>18</sup>

When a ballistic pendulum diagnostic<sup>2</sup> is used, as it is here, special care must be taken that events beyond the focal-spot periphery do not influence the experimental results. Such events, if significant, could not only complicate interpretation of the results but could make them irrelevant to laser fusion, since a fusion pellet surface has no edges. For many diagnostics the finiteness of the laser spot is not a major concern since

the phenomenon investigated requires high energies that exist only within the focal spot or the diagnostic has time or space resolution. But a pendulum is time and space integrating, and a small amount of energy can easily heat large amounts of mass to produce a large momentum. Small amounts of such extraneous energy may be provided by thermal conduction through the focal-spot periphery, by plasma flow along the target surface, or by radiation from the plasma plume. The situation is further complicated since these heating mechanisms may vary with laser-spot size, energy, or irradiance. We have observed, in fact, that under some circumstances the momentum of material from beyond the focal-spot region is 7 times as large as the momentum from within the focal-spot region.<sup>2</sup> For these reasons we ordinarily use only disk targets with the pendulum diagnostic.

Angular distributions of the ablation plasma energy  $E(\theta)$ , momentum  $p(\theta)$ , and velocity  $\bar{u}(\theta)$  for an isolated disk target are shown in Fig. 14;  $\bar{u}$  is a mean velocity unfolded from ion-collector traces.<sup>2</sup> Angular distributions from various disk (0.3 to 1.2 mm diameter) and wide foil targets have similar shapes. All detectors are in the plane of incidence and cylindrical symmetry about the target normal is assumed. From such angular distributions we determine the ablation pressure  $\mathcal{P}_\perp = P_\perp / \tau A$ , mass ablation rate  $\dot{m} = m_a / \tau A$ , and ablation velocity  $u_\perp = P_\perp / m_a$  where  $m_a$  is the ablated mass,  $\tau$  is the FWHM pulse duration, and  $P_\perp$  is the normal component of the total momentum  $P$  obtained by integrating  $p(\theta)$  over all solid angles. The letter  $A$  in the definition of  $\mathcal{P}_\perp$  and  $\dot{m}$  represents either the surface area of a disk target or, for a foil target, the focal-spot area containing 90% of the laser energy. In the latter case, the focal-spot diameters are chosen to be large ( $\approx 1$  mm) so that extraneous focal-spot-edge effects are minimized.

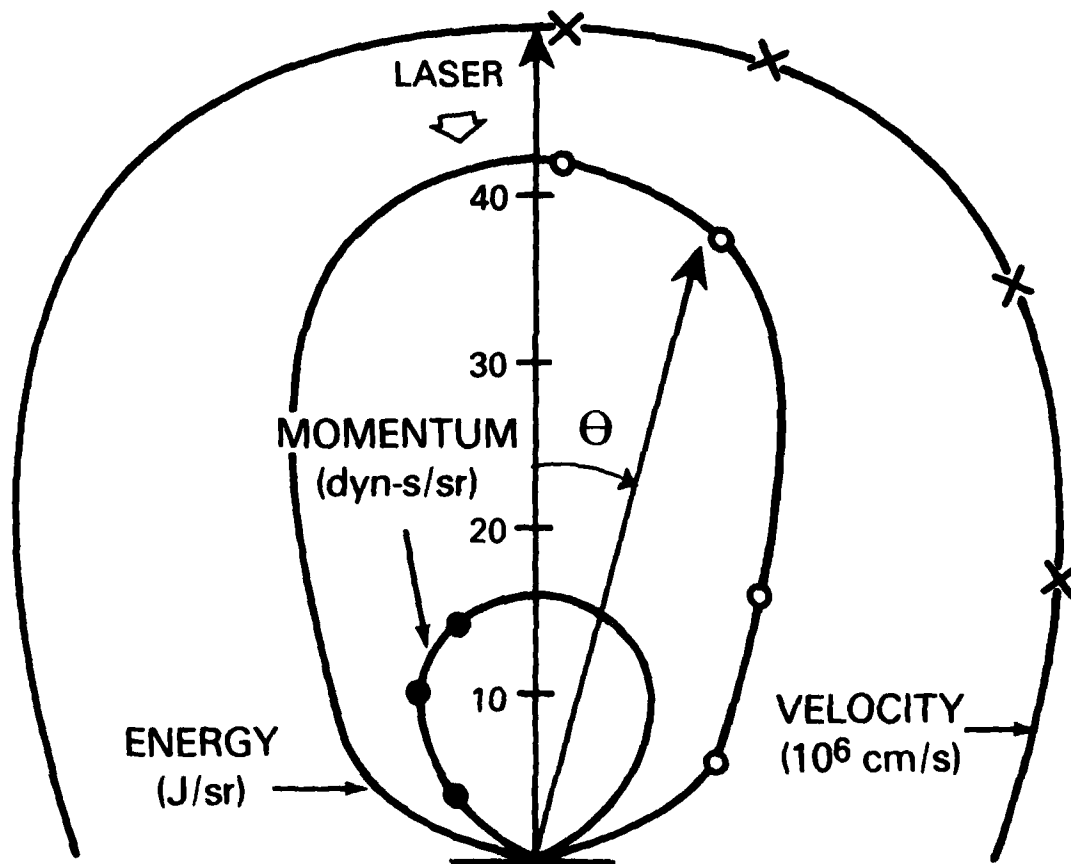


Fig. 14 — Distribution of blowoff velocity, energy and momentum measured with time-of-flight ion collectors, plasma calorimeters, and ballistic pendula respectively. The target is a 1.2-mm diameter CH disk irradiated at  $3 \times 10^{12}$  W/cm<sup>2</sup>.

Scaling of ablation pressure with absorbed irradiance  $\mathcal{P}_1 \propto I_a^{0.8}$  is shown in Fig. 15a.<sup>2,5</sup> Momentum (pressure) in the case of disk targets is determined in two independent ways: first directly, using the pendulum array and second, indirectly, using the energy from plasma calorimeters and velocity data from time-of-flight detectors; wide foil results use the latter method only. Agreement between all these independent measurements increases our confidence in the results. The scalings in the absorbed irradiance of the ablation velocity  $u_1 \propto I_a^{0.2}$ , and the mass ablation rate  $\dot{m} \propto I_a^{0.6}$  are shown in Fig. 15b.

The momenta of the ablation plasma (Fig. 15a) and the momenta of the accelerated targets, inferred from the velocity measurements in Section III, balance. For example, the target momentum for the cases in Fig. 6 is about 0.7 of the ablation plasma momentum. Similar agreement was obtained on a few shots where the target velocities and the ablation plasma momenta were simultaneously measured.

Figure 15 also shows that the measured ablation parameters agree well with like quantities computed with our hydrodynamic code. In this code, the time averaged ablation parameters are calculated by computing the total mass and momentum moving away from the target late enough in the run ( $\approx 14$  nsec) so that little further mass or momentum is added to the plasma. This is done so that the computed quantities are nearly the same as the quantities measured experimentally. The calculated scalings are:  $\mathcal{P}_1 \propto I_a^{0.75}$ ,  $u_1 \propto I_a^{0.24}$ , and  $\dot{m} \propto I_a^{0.55}$ .

Table I compares our ablation results to other published theories. All of these theories assume a steady or quasi-steady ablation plasma flow which is described by conservation of mass, energy, and momentum: but they differ in other details. Some theories (Kidder, Caruso and Gratton),<sup>19,20</sup> which are in planar geometry, neglect details of the

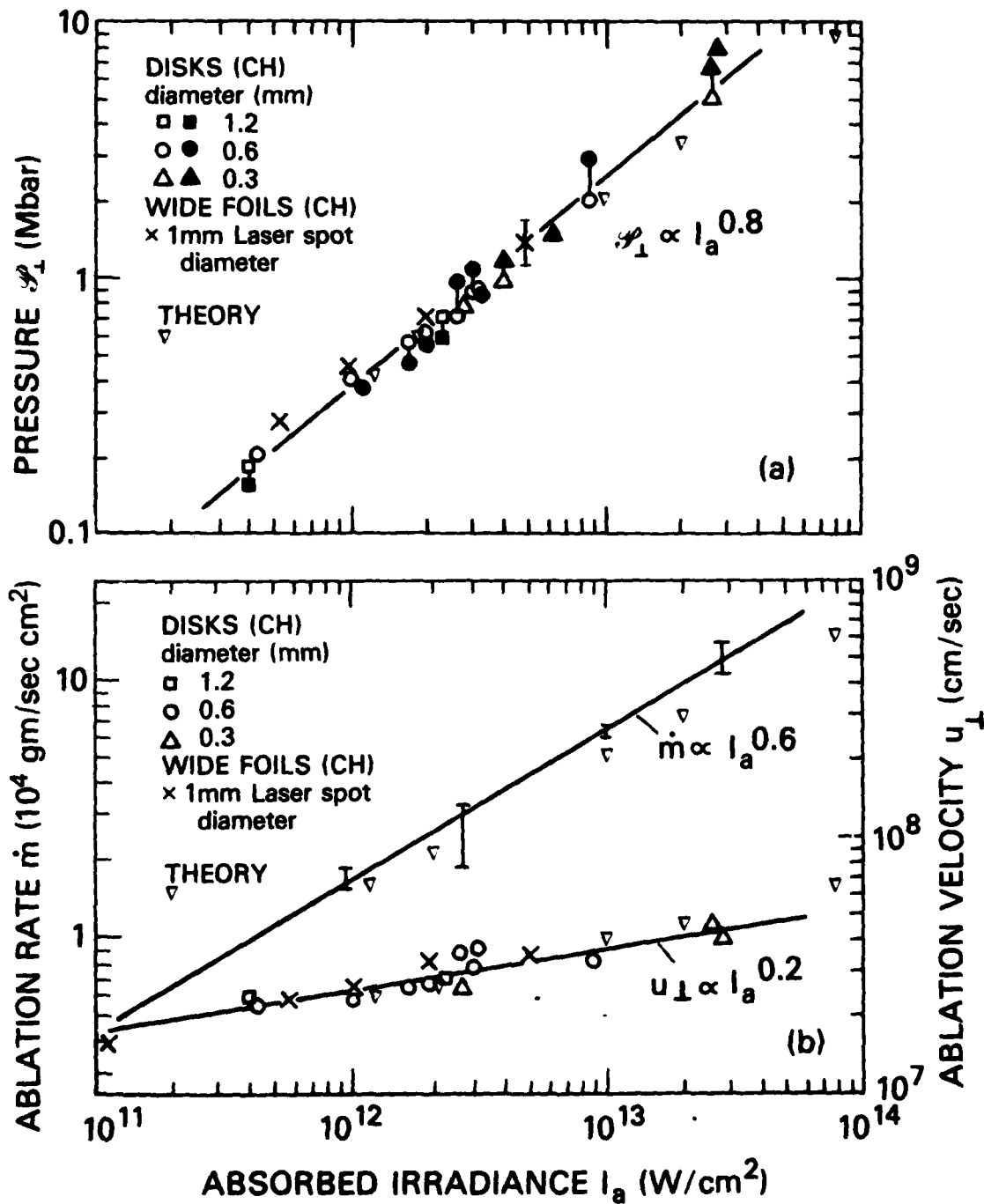


Fig. 15 - (a) Ablation pressure versus absorbed laser irradiance for disks and wide foil targets. The data denoted by  $\bullet$ ,  $\blacksquare$ ,  $\blacktriangle$  are inferred using momentum measured with ballistic pendula. The data  $\circ$ ,  $\square$ ,  $\triangle$  are obtained using calorimeter and time-of-flight measurements. (b) Mass ablation rate and normal ablation velocity  $u_{\perp}$  versus absorbed irradiance  $I_a$ . Points are obtained using calorimeters and time-of-flight detectors. The laser pulse duration in (a) and (b) is 4-nsec FWHM.

TABLE 1

Comparison of experiment to theoretical scaling laws. Table entries are the exponents  $b$  of  $y \propto I_a^b$  where  $y$  is an ablation parameter, and  $I_a$  the absorbed irradiance. The theories may be found in references 19-26.

THEORY	$\mathcal{P}_\perp$	$u_\perp$	$\dot{m}$
KIDDER	0.75	0.25	0.50
CARUSO	0.75	0.25	0.50
AHLBORN	0.78*	0.22*	0.56*
JARBOE	0.66**	0.33**	0.33**
PUELL	0.78	0.22	0.56
NEMCHINOV	0.78	0.22	0.56
GITOMER			0.56
MAX	0.57	0.09	0.48
EXPERIMENT	0.8	0.2	0.6

\* $\eta^{\pm 1/9}, \eta^{2/9}$  IN AHLBORN'S EXPRESSIONS HAVE BEEN TREATED AS CONSTANTS.  $\eta$  IS THE ABSORPTION FRACTION.

\*\*JARBOE ET AL. DERIVE EXPLICITLY A RELATION FOR  $u_\perp$  ONLY. TO GET THE OTHER TWO QUANTITIES WE USED THE RELATIONS  $\mathcal{P}_\perp \propto n_c u_\perp^2$  AND  $\dot{m} \propto n_c u_\perp$  IMPLIED BY HIS THEORY;  $n_c$  IS THE CRITICAL DENSITY.

absorption and energy transport to the ablation layer. They also assume that all of the absorbed energy supports the expansion of the ablation plasma, and that the underdense plasma expands with sonic velocity. Another theory (Jarboe, et al.)<sup>21</sup> assumes sonic flow at the critical surface and one (Ahlborn, et al.)<sup>22</sup> eliminates the sonic flow hypothesis altogether. Divergent plasma flow from planar targets was included by Puell<sup>23</sup> who treated plasma hydrodynamics in planar geometry using a model similar to Refs. 19, 20, but considered plasma expansion when calculating absorption of laser light and the temperature at the sonic radius. Scalings of ablation parameters with irradiance in spherical geometry were determined by Nemchinov<sup>24</sup> who neglected thermal transport. Scaling of the mass ablation rate was determined by Gitomer, et al.<sup>25</sup> who included thermal transport but assumed that the sonic radius does not vary with irradiance. The effects of inhibited thermal conductivity in spherical geometry (at irradiances higher than ours) upon ablation was considered by Max, et al.<sup>26</sup>

Our results agree with all the theories except that of Max, et al. which assumes strongly inhibited thermal transport, and that of Jarboe et al. who fix the sonic flow point at critical density and do not let the exhaust density vary with irradiance.

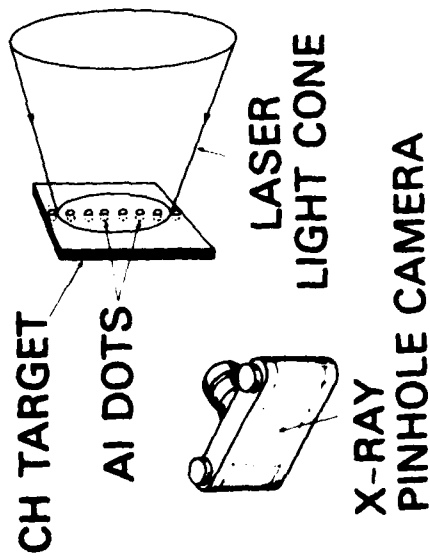
Until now, we have discussed measurements of ablation plasma parameters far from the target surface, i.e. after the parameters reached their asymptotic values. It is, of course, desirable to also know the hydrodynamic development of these quantities as the plasma flows away from the target. In particular, if the results of our experiments are to be extrapolated to spherical geometry, then the difference between plasma flow from our planar targets and spherical pellets must be taken into account. Toward this end, we have

developed a tracer technique that lets us spatially resolve the plasma flow from a target surface.<sup>6</sup> Using this method we can also track plasma flow from nonuniformly irradiated targets so that smoothing effects may be studied.

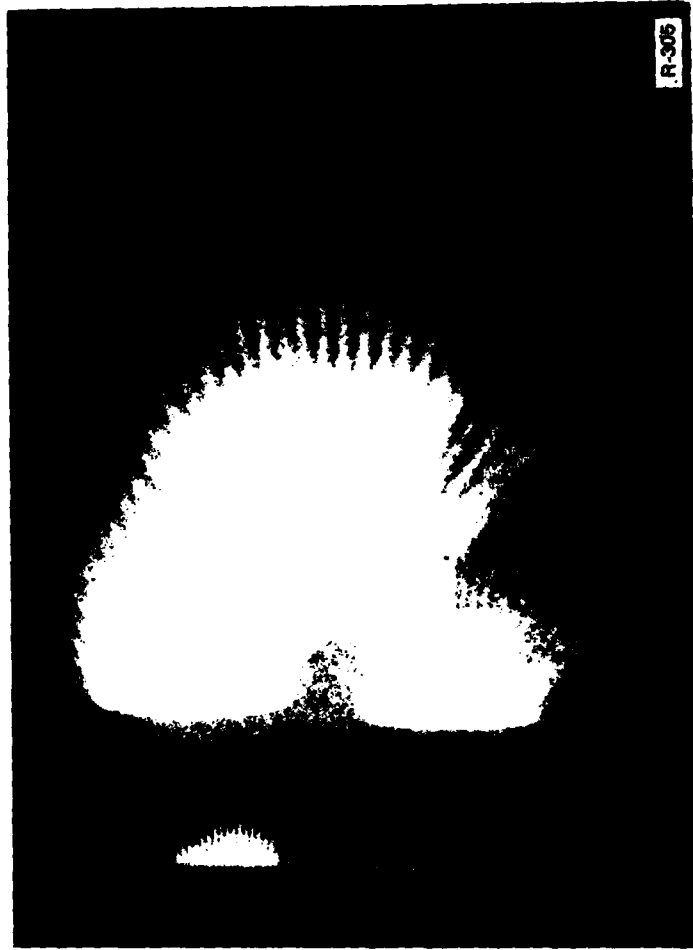
The arrangement for this experiment is shown in Fig. 16a. An x-ray pinhole camera is placed to view edge-on a polystyrene (CH) target with a row of small Al dots (0.5  $\mu\text{m}$  thick, 25  $\mu\text{m}$  diameter, spaced 50  $\mu\text{m}$  apart) imbedded in it. When the target is irradiated both the aluminum and the polystyrene ablate from its surface. However, since the aluminum is a much stronger emitter of x rays in the spectral band of the pinhole camera ( $>1$  keV) than polystyrene, the presence of aluminum ions in the plasma flow is identified by the presence of strong x-ray emission. We assume that the perturbation of the flow pattern by the aluminum tracer is small. This assumption is reasonable since for a given electron density  $n_e$  in the ablation plasma the fully ionized ion mass density  $\rho_i$  for Al and CH targets differ only by 12% ( $\rho_i = n_e M/Q$ , where  $Q$  and  $M$  are the ion charge and mass respectively). Also, the speed of Al and CH target ions, measured with time-of-flight ion collectors, is the same.

Figure 16b is a photograph of the plasma flow from a target irradiated by a nonperturbed laser beam. The five images in the figure result from a five pinhole array (5-55  $\mu\text{m}$ ) through which the target was photographed. It is evident from Fig. 16b that the ablation plasma flow is reminiscent of a steady state fluid flow from a circular orifice. Note that the plasma flow is planar near the target surface, and that distinct regions of the target map into distinct solid angles.

In Section III it was shown that the velocity profiles of accelerated targets were, under certain conditions, smoother than expected given the



(a)



(b)

Fig. 16 - (a) Experimental setup to spatially resolve plasma flow near the target surface. (b) Spatially resolved plasma flow near the target surface. The five images are from five pinholes in the camera.

irradiance nonuniformity. We surmised that these smoother velocity profiles resulted from ablation pressures which were themselves smoothed by lateral heat flow in the ablation plasma. Such smoothing in the ablation plasma is also observed using the tracer technique. Figure 17a shows spatially resolved plasma flow from a thick CH target irradiated by a laser beam distorted as in Fig. 11. The average irradiance is,  $3 \times 10^{12} \text{ W/cm}^2$ , the nonuniformity depth  $I_{\text{max}}/I_{\text{min}}$  is about 8, and the nonuniformity width is 220- $\mu\text{m}$  FWHM. Under these conditions no significant ablation smoothing is expected and none is seen here. However, smoothing is expected and seen in Fig. 17b where the average irradiance is raised by a factor of 2, the nonuniformity depth is reduced to about 6, and the nonuniformity width is reduced to 140- $\mu\text{m}$  FWHM. Under these conditions lateral energy flow from the directly irradiated regions into the central shaded region ablates the target surface there and causes distinct streamlines of plasma to emanate from the shaded region. These streamlines are compressed only slightly by the surrounding plasma which indicates that the pressures in the shaded and unshaded regions are comparable, and qualitatively confirms the previous results. Quantitative measurements of plasma conditions in the shaded region are the subject of a future study.

#### V. CONCLUSION

In this work we used ablatively accelerated planar targets to model the dynamics of large, hollow, ablatively driven fusion pellets. The velocities and velocity profiles of the dense regions of highly accelerated planar targets were measured. Despite two-to-one, short-scalelength laser nonuniformities, we did accelerate thin, relatively uniform, and cool targets to 160 km/sec. We have also measured an increase in irradiance profile smoothing with

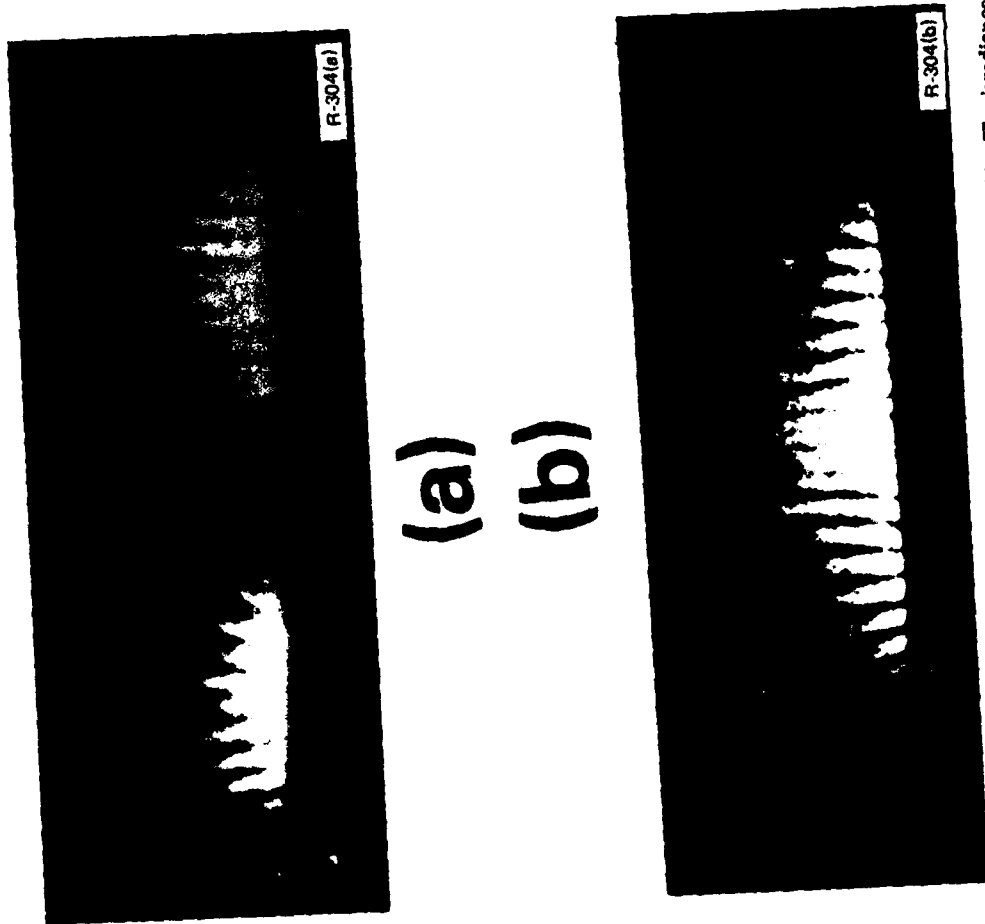
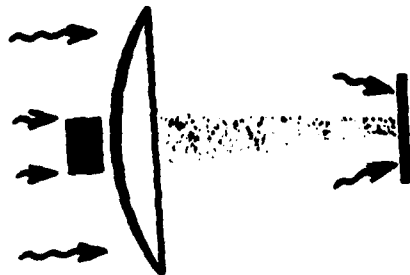


Fig. 17 -- Ablation plasma flow from thick CH targets irradiated by a structured laser profile. The irradiance conditions are: (a) Mean irradiance of  $3 \times 10^{12} \text{ W/cm}^2$ ,  $I_{\text{max}}/I_{\text{min}} \approx 8$ ,  $220\text{-}\mu\text{m}$  FWHM dip. (b) Mean irradiance of  $6 \times 10^{12} \text{ W/cm}^2$ ,  $I_{\text{max}}/I_{\text{min}} \approx 6$ ,  $140\text{-}\mu\text{m}$  FWHM dip. Mean irradiance is changed here by reducing the laser spot diameter.

increasing laser irradiance. This is encouraging for laser fusion. However, the behavior of targets with multimillimeter density and nonuniformity scalelengths that are typical of fusion scenarios is not yet known.

We also made simultaneous measurements of the ablation pressure  $\mathcal{P}_1$ , ablation rate  $m$ , and ablation velocity  $u_1$ . In these measurements we utilized large laser spots and disk targets so that our results are not sensitive to focal-spot-edge effects. We found that  $\mathcal{P}_1 \propto I_a^{0.8}$ ,  $m \propto I_a^{0.6}$ , and  $u_1 \propto I_a^{0.2}$  where  $I_a$  is the absorbed irradiance. Also, the ablation plasma momenta and the momenta of ablatively accelerated targets balance. These results agree with a planar geometry fluid code that uses classical transport physics.

#### VI. ACKNOWLEDGEMENTS

We acknowledge useful discussions with S. Bodner, H. Griem and R. Lehmberg. The technical assistance of M. Fink, N. Nocerino, L. Seymour and E. Turbyfill is greatly appreciated.

This work was supported by the Department of Energy and the Office of Naval Research.

## REFERENCES

- (a) Mission Research Corporation, Alexandria, VA.
1. J.H. Nuckolls, R.O. Bangerter, J.D. Lindl, W.C. Mead, and Y.L. Pan, European Conference on Laser Interaction with Matter, Oxford England Sept. 1977.
  2. J. Grun, Naval Research Laboratory Memorandum Report No. 4491 (1981).
  3. S.P. Obenschain, J. Grun, B.H. Ripin and E.A. McLean, Phys. Rev. Lett. 46, 1402 (1981).
  4. R.R. Whitlock, S.P. Obenschain, J. Grun, J. McMahon and B.H. Ripin, Proceedings of the Topical Conference on Symmetry Aspects of Inertial Fusion Implosions, May 27-28, 1981, Naval Research Laboratory, Washington, D.C.
  5. J. Grun, R. Decoste, B.H. Ripin, and J.H. Gardner, Appl. Phys. Lett. 39, 545 (1981).
  6. M.J. Herbst, and J. Grun, Phys. Fluids 24, 1917 (1981).
  7. J.M. McMahon, R.P. Burns, T.H. DeRieux, R.A. Hunsicker, and R.H. Lehberg, IEEE J. Quantum Electron. QE-17, 1629 (1981).
  8. R. Decoste, S.E. Bodner, B.H. Ripin, E.A. McLean, S.P. Obenschain, and C.M. Armstrong, Phys. Rev. Lett. 42, 1673 (1979); B.H. Ripin, R. Decoste, S.P. Obenschain, S.E. Bodner, E.A. McLean, F.C. Young, R.R. Whitlock, C.M. Armstrong, J. Grun, J.A. Stamper, S.H. Gold, D.J. Nagel, R.H. Lehberg, and J.M. McMahon, Phys. Fluids 23, 1012 (1980); 24, 990 (E) (1981).
  9. B.H. Ripin in NRL Memorandum Report No. 3315, Ch. II, (August 1976), S.E. Bodner, ed.

10. E.A. McLean, S.H. Gold, J.A. Stamper, R.R. Whitlock, H.R. Griem, S.P. Obenschain, B.H. Ripin, S.E. Bodner, M.J. Herbst, S.J. Gitomer, and M.K. Matzen, Phys. Rev. Lett. 45, 1246 (1980).
11. B.H. Ripin, S.E. Bodner, S.H. Gold, H.R. Griem, J. Grun, M.J. Herbst, R.H. Lehmborg, E.A. McLean, J.M. McMahon, S.P. Obenschain, J.A. Stamper, R.R. Whitlock, and F.C. Young, presented at the CLEOS/ICF'80 Topical Meeting on Inertial Confinement Fusion, February 27, 1980, San Diego, CA.
12. J.H. Gardner, and S.E. Bodner, Phys. Rev. Lett. 47, 1137 (1981).
13. One of the authors has also observed an increase of opacity in an initially transparent single target irradiated by a laser. S. Gold and E.A. McLean (to be published).
14. J.H. Nuckolls, L. Wood, A. Thiessen, and G. Zimmerman, Nature 239, 193 (1972).
15. S.E. Bodner, Naval Research Laboratory Memorandum Report No. 4453 (1981) (to be published in J. of Fusion Energy).
16. N.A. Ebrahim, C. Joshi, D.M. Villeneuve, N.H. Burnett, and M.C. Richardson, Phys. Rev. Lett. 43, 1996 (1979).
17. C.M. Armstrong, B.H. Ripin, F.C. Young, R. Decoste, R.R. Whitlock, and S.E. Bodner, J. Appl. Phys. 50 (8), 5233 (1979).
18. F.C. Young (private communication).
19. R.E. Kidder, Nuclear Fusion, 8, 3 (1968).
20. A. Caruso, and R. Gratton, Plasma Phys. 10, 867 (1968).
21. T.R. Jarboe, W.B. Kunkel and A.F. Lietzke, Phys. Fluids 19, 1501 (1976).
22. B. Ahlborn and M.H. Key, U. of British Columbia Lab. Report No. 73 (1980).
23. H. Puell, Z. Naturforsch 25a, 1807 (1970).
24. I.V. Nemchinov, J. Appl. Math. Mech. 31, 320 (1967).

25. S.J. Gitomer, R.L. Morse, and B.S. Newberger, *Phys. Fluids* 20, 234 (1977); Scaling of the mass ablation rate may be determined from this paper if  $r_s$  (the sonic radius) is assumed constant - S.J. Gitomer (private communication).
26. C.E. Max, C.F. McKee, and W.C. Mead, *Phys. Rev. Lett.* 45, 28 (1980).

DISTRIBUTION LIST

USDOE (194 copies)  
Technical Information Center  
P.O. Box 62  
Oak Ridge, TN 37830

National Technical Information Service (24 copies)  
U.S. Department of Commerce  
5285 Port Royal Road  
Springfield, VA 22161

NRL, Code 2628 (35 copies)

NRL, Code 4730 (200 copies)

NRL, Code 4700 (26 copies)

USDOE (6 copies)  
Division of Laser Fusion  
Washington, D.C. 20545  
Attn: Dr. R. Schriever  
    Dr. S. Kahalas  
    Dr. T. Godlove  
    Dr. S. Barrish  
    Dr. L. Killion  
    Dr. K. Gilbert

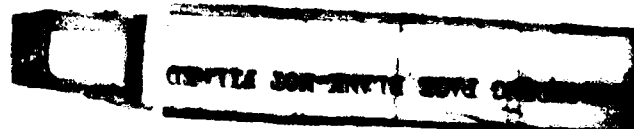
Defense Technical Information Center  
Cameron Station  
5010 Duke Street  
Alexandria, VA 22314

Naval Sea Systems Command  
PMO-405-23  
Washington, D.C.  
Dr. J. Stregack

Mr. Len Kojm  
MS-7E054  
Dept. of Energy  
Washington, D.C. 20585

Lawrence Livermore Laboratory  
P.O. Box 808  
Livermore, CA 94551  
Attn: Dr. D. Attwood, L481  
    Dr. J.F. Holzrichter, L545  
    Dr. W. Kruer, L545  
    Dr. A. Langdon, L388  
    Dr. B. Lasinski, L32  
    Dr. J. Lindl, L32  
    Dr. C. Max, L545  
    Dr. V. Rupert  
    Dr. D. Phillion  
    Dr. L. Coleman

Dr. J. Nuckolls  
Dr. J. Emmett  
Dr. W. Mead  
Dr. R. More  
Dr. N. Ceglio  
Dr. R. Kidder



KMS Fusion  
3941 Research Park Drive  
P.O. Box 1567  
Ann Arbor, MI 48106  
Attn: Dr. F. Mayer  
Dr. R. Johnson  
Dr. R. Berger  
Dr. E. Storm  
Dr. T. Spieziali  
Dr. A. Glass

TRW Corp.  
1 Space Park  
Redondo Beach, CA  
Attn: Dr. D. Arnush  
Dr. J. Thompson

W.J. Schaefer Assoc.  
1901 N. Fort Myer Drive., Suite 800  
Arlington, VA 22209  
Attn: Dr. E. Gerry

JAYCOR  
San Diego, CA  
Attn: Dr. N. Krall

Fusion Power Assoc.  
2 Professional Drive  
Suite 248  
Gaithersburg, MD 20760  
Attn: Dr. Steve Dean, President

Physics International  
2700 Merced Street  
San Leandro, CA 94577  
Attn: A.J. Toepfer  
E. Goldman  
G. Dahlbacka

Mission Research Inc.  
Santa Barbara, CA  
Attn: Dr. C. Longmire

Science Applications Inc.  
1710 Goodridge Drive  
McLean, VA 22102  
Attn: Dr. Walter Sooy

Institut fur Plasmaphysik  
8046 Garching  
Bei Munchen  
West Germany  
Attn: Dr. R. Sigel  
Dr. K. Eidmann

National Research Council  
Division of Physics  
100 Sussex Drive  
Ottawa K1A-0R6, Canada  
Attn: Dr. J. Alcock  
Dr. N. Burnett

University of Quebec  
INRS Energie  
Case Postale 1020  
Varenes, Quebec  
Attn: Dr. T. Johnston  
Dr. R. Decoste  
Dr. H. Pepin

Laboratoire de Physique des  
Milieux Ionises  
Ecole Polytechnique  
17, Rue Descartes  
75230 Paris Cedex 05  
France  
Attn: Dr. E. Fabre  
Dr. J. Virmont

University of British Columbia  
Dept. of Physics  
Vancouver, Canada V6T1W5  
Attn: Dr. Boye Ahlborn

Institute for Laser Engineering  
Osaka University  
Suite Osaka, 565  
Japan  
Attn: Dr. C. Yamanaka  
Dr. S. Nakai  
Dr. T. Mochizuki  
Dr. Y. Izawa  
Dr. H. Matoba  
Dr. T. Yabe  
Dr. K. Nishihara  
Dr. K. Mima  
Dr. H. Azechi  
Dr. T. Yamanaka

Shanghai Institute of Optics and  
Fine Mechanics  
Academia Sinica  
Shanghai, PRC  
Attn: Prof. Gan Fu-xi  
Prof. Yu Wen-yan  
Prof. Xu Zhi-zhan  
Prof. Deng Xi-ming  
Prof. Tan Wei-han  
Mr. Pan Cheng-min

Los Alamos Scientific Laboratory  
P.O. Box 1663  
Los Alamos, NM 87545  
Attn: Dr. D. Forslund  
Dr. S. Gitomer  
Dr. J. Kindel  
Dr. C.J. Elliot  
Dr. S. Rockwood  
Dr. D. Giovanelli  
Dr. T. Tan  
Dr. G. Kyrala  
Dr. S. Singer  
Dr. P. Goldstein  
Dr. W. Ehler

Sandia Laboratory  
P.O. Box 5800  
Albuquerque, NM 87115  
Attn: Dr. K. Matzen  
Dr. J. Anthes  
Dr. R. Palmer  
Dr. G. Yonas  
Dr. J.R. Asay

Maxwell Laboratory Inc.  
8835 Balboa Ave.  
San Diego, CA 92123  
Attn: Dr. J. Pearlman  
Dr. A. Kolb

Air Force Weapons Lab.  
Kirkland AFB  
New Mexico 87117  
Attn: Dr. A. Guenther  
Dr. D. Woodall

Lawrence Berkeley Lab  
1 Cyclotron Road  
Berkeley, CA 94720  
Attn: Dr. C. Kim

University of Alberta  
Dept. of Electrical Engineering  
Edmonton, Canada  
Attn: Dr. A. Offenberger

University of California at  
San Diego  
Department of Physics  
La Jolla, CA 92037  
Attn: Dr. K. Brueckner  
Dr. W. Thompson  
Dr. S.C. Lin

University of Maryland  
Department of Physics and Astronomy  
College Park, MD 20740  
Attn: Dr. C.S. Liu  
Dr. E. Ott  
Dr. H. Griem  
Dr. D. Tidman

University of Rochester  
Laboratory for Laser Energetics  
Rochester, NY 14627  
Attn: Dr. B. Yaakobi  
Dr. J. Soures  
Dr. M. Richardson  
Dr. S. Craxton  
Dr. J. Eastman  
Dr. E. Thorsos  
Dr. W. Seka  
Dr. R. McCrory

University of California  
Department of Physics  
Los Angeles, CA 90024  
Attn: Dr. F. Chen  
Dr. N. Luhmann  
Dr. A. Wong  
Dr. B. Fried  
Dr. R. Stenzel  
Dr. W. Gekelman

Massachusetts Inst. of Technology  
Cambridge, MA  
Attn: Dr. Ronald Davidson

University of Illinois  
Nuclear Engineering Laboratory  
Urbana, IL 61801  
Attn: Dr. G. Miley

North Carolina State University  
Dept. of Physics  
Raleigh, NC 27607  
Attn: Dr. Carter Armstrong

Cornell University  
Laboratory for Plasma Studies  
Upson Hall  
Ithaca, NY 14853  
Attn: Dr. C. Wharton  
Dr. R. Sudan  
Dr. D. Hammer  
Dr. H. Fleishman  
Cornell University  
School of Applied & Engineering Physics  
College of Engineering  
Ithaca, NY 14853

Institute of Atomic Energy  
Academia Sinica  
Beijing, PRC  
Attn: Prof. Hong Run-sheng  
Prof. Wang Nai-yan

CEA  
Centre d'etudes de Limeil  
Villeneuve St. Georges 94190  
France  
Attn: Dr. M. Decroisette  
Dr. Coutant

Soreq Nuclear Center  
Yavne, Israel  
Attn: Dr. A. Krumbejn  
Dr. H. Zmora  
Dr. S. Jackel  
Dr. B. Arad  
Dr. H. Loebenstein  
Dr. S. Eliezer

Electro Technical Laboratory  
1-1-4 Umezono  
Sakura-Mura  
Nihari-gun  
Ibaraki  
Japan 305  
Attn: Dr. M. Sugiura

AWRE  
Aldermaston, England  
Attn: Dr. J. Weale  
Dr. P. Flynn

1st Fisica Applicata  
via Bassi 6 Pavia  
Italy  
Attn: Dr Sergio Morosi

Zentralinstitut fur Optik and Spektroskopie  
DDR-1199 Berlin-Adlershof  
Rudower Chaussee 6  
West Germany  
Attn: Prof. G. Wallis  
Prof. K. Junge

INTERNAL DISTRIBUTION

Code 4740 R. Parker  
V. Granatstein  
Code 4040 D. Book  
J. Boris  
M. Emery  
J. Gardner

Rutherford Laboratory  
Chilton, Didcot  
Oxon, OX11 0QX  
ENGLAND

Attn: Dr. M. Key  
Dr. A. Gibson  
Dr. T. Raven  
Dr. P. Rumsby  
Dr. J. Kilkenny  
Dr. R. Evans

Library  
Institut fur Plasmaforschung  
Universitat Stuttgart  
Pfaffenwaldring 31  
7000 Stuttgart 80, West-Germany